10. Doppler Tracking

Experiment MA-089

G. C. Weiffenbach,[a†] M. D. Grossi,[a] and P. W. Shores[b]

ABSTRACT

The Doppler Tracking Experiment was designed to test the feasibility of improved mapping of the Earth's gravity field by means of the low-low satellite-to-satellite tracking method and to observe variations in the electron density of the ionosphere between two spacecraft. Data were taken between 01:01 and 14:37 UT on July 24, 1975. Baseline data taken earlier, while the docking module was still attached to the command and service module, indicated that the equipment operated satisfactorily.

The ionospheric data contained in the difference between the Doppler signals acquired at the two experimental frequencies are of excellent quality. The data represent valuable satellite-to-satellite observations, never made before, of wave phenomena in the ionosphere. The gravity data were corrupted by an unexpectedly high noise level of as-yet-undetermined origin, with periods greater than 150 seconds, which prevented unambiguous identification of gravity-anomaly signatures.

INTRODUCTION

Interest has recently focused on mass density anomalies with scale sizes of 100 to 700 km in the upper mantle of the Earth. It is likely that these anomalies are important factors in the physics of the mantle and plate tectonics and in the reconstruction of important aspects of the Earth's evolution, such as continental drift. Small-scale anomalies near the surface of the Earth have been studied for many years by means of surface gravimetry; and large-scale anomalies, greater than 2000 km, have been investigated for almost 20 years by observing artificial-satellite orbit perturbations. The spacecraft-to-spacecraft Doppler Tracking Experiment (MA-089) conducted by the Smithsonian Astrophysical Observatory (SAO) during the Apollo-Soyuz Test Project (ASTP) mission was designed to determine gravity features having an intermediate horizontal scale of 250 to 1000 km. The ASTP mission was particularly suitable for this experiment because it provided two platforms with a controlled separation within the same orbit at an altitude low enough for enhanced sensitivity to these short-wavelength gravity anomalies.

The experiment consisted of measuring (by means of a phase-coherent, dual-frequency, very-high-frequency link) the relative velocity, or Doppler shift, between the docking module (DM) and the command and service module (CSM). Both orbiting at a height of 220 km, these two modules had an initial separation of 310 km, which increased to 430 km by the end of the data take. From their relative-velocity data, localized anomalies in the Earth's gravitational field should be measured with a threshold sensitivity of better than 0.15 mm/sec^2 (15 mgal). The geometric range rate induced by the ionosphere was removed by the dual-frequency (162 and 324 MHz) correction.

[a]Smithsonian Astrophysical Observatory.

[b]NASA Lyndon B. Johnson Space Center.

[†]Principal Investigator.

A secondary goal of the experiment was to measure changes in the integrated electron concentration and other ionospheric properties along a radio path between the CSM and the DM and between the DM and the ground.

Since the time available for the Doppler Tracking Experiment was limited to 12 hours, complete global coverage was not expected to be possible; therefore, the experiment was meant to serve solely as a feasibility demonstration.

THEORY

Measuring the Earth's Gravity Field

The structure of the Earth's gravity field has been of considerable scientific interest for some time because it provides one of the few available clues to the internal distribution of mass in the Earth. The recent development of the plate-tectonics hypothesis has placed added emphasis on the need for information on those particular features in the gravity field that have horizontal wavelengths of 100 to 700 km.

Evidence from studies of seismic-wave propagation shows that the outer portion of the Earth consists of (1) a high-velocity zone, the lithosphere, which generally includes the crust and uppermost mantle, has significant strength, and is approximately 50 to 80 km thick under the oceans and somewhat thicker under the continents; (2) a low-velocity zone, the asthenosphere, which is a layer of low effective strength on a geologic time scale and extends from the base of the lithosphere to a depth of several hundred kilometers; and (3) the lower remaining portion of the mantle, the mesosphere, which may have strength and is relatively passive in tectonic processes.

The plate-tectonics concept is based on the observation that large blocks or plates of the rigid lithosphere, some thousands of kilometers in horizontal extent, appear to be moving ("floating" on the yielding asthenosphere) with respect to one another at average long-term rates of approximately 1 to 15 cm/yr (ref. 10-1). One manifestation of this plate motion is continental drift. Most large earthquakes, volcanic activity, mountain building, and tsunami generation, plus some terrestrial mineral resources, are located at the boundaries of the lithospheric plates. In fact, nearly all large-scale geological and geophysical phenomena occurring on the Earth's surface appear to be intimately related to this global pattern of plate motions. Thus, the subject of plate tectonics is of considerable scientific and practical interest. However, no satisfactory theory of the mechanism or mechanisms producing plate motion is available. It is very probable that both thermal convection and chemical convection in the asthenosphere are involved in some way, and most current theories include one or both processes. In any event, there is little question that knowledge of the density field in the upper portion of the Earth, to a depth of 700 km or so, would be of considerable importance in determining the basic mechanisms underlying plate motion.

The distribution of mass within the Earth uniquely determines the external gravity field. Hence, measurements of the latter contain information on the density field (although it should be noted that the external field does not define the unique internal mass distribution). As a rough approximation, a density anomaly within the Earth will produce a lateral variation in the external gravity field with a scale comparable to the depth of the anomaly. Thus, the density field within the upper mantle at depths of approximately 100 to 700 km will generally be reflected in horizontal variations of the gravity field having wavelengths of 100 to 700 km. This fact suggests that measurements of intermediate-wavelength (100 to 1000 km) features in the gravity field will be fundamental to advancing the understanding of plate tectonics.

The intermediate-wavelength structure of the Earth's gravity field is of interest for another reason. The surface of the ocean contains topographic signatures of current systems, eddies, storm surges, tsunamis, barometric loading, etc., all of which are of considerable practical importance. There is great interest in developing methods for maintaining frequent surveillance of these phenomena over the world's ocean. One very promising approach is to map the topography

of the ocean with satellite-borne radar altimeters. The third Geodetic Earth Orbiting Satellite (GEOS-3), launched by NASA in April 1975, has such an altimeter.

However, the mean-sea-level surface also contains the topographic imprint of the Earth's gravity field, i.e., the geoid. Geoid undulations must be mapped and removed from the measured ocean topography before it will be possible to identify the signatures of oceanographic parameters uniquely. All the previously mentioned oceanic features have topographic structures with significant lateral components in the range 100 to 1000 km. The estimated geoid accuracy needed for this purpose is 10 cm in geoid height.

Measuring the Earth's gravity field has been a continuing occupation of geodesists for many years. The traditional method has been to use gravimeters at fixed locations in land areas and onboard ships, submarines, and, more recently, aircraft. This method provides accurate measurements of the detailed structure of the gravity field, particularly on land. However, surface gravimetry has several deficiencies: the cost and time involved in covering large geographic areas (particularly in rough terrain), the reduced accuracy of gravimeters on mobile platforms, and the loss in accuracy of large-scale gravity variations synthesized from gravimeter data.

More recently, the structure of the gravity field has been calculated by way of orbital dynamics from accurate tracking of artificial satellites. Because satellite orbits are uniquely determined by the forces acting on the satellite and because gravity is by far the dominant force, the gravitational force can be inferred from the observed orbits and an appropriate orbit theory. This orbital-dynamics approach has been used successfully to measure the large-scale structure of the gravity field with considerable accuracy. However, the orbital-dynamics approach is not suitable for measuring intermediate- or short-wavelength gravity-field features. Specifically, spherical-harmonics terms of degree higher than 20 are impractical, both because of the rapidly increasing complexity of the theory and its computer mechanization and because of the need for many more satellites in different orbits. Thus, this method is restricted, for practical reasons, to gravity features having horizontal wavelengths greater than 2000 km.

The Gravity Field From Satellite-to-Satellite Velocity Measurements

Artificial satellites can be used in another way to measure intermediate-sized gravity features. Employed in the SAO Doppler Tracking Experiment, the method is based on calculating the gravitational force acting on a spacecraft directly from changes in its measured velocity. Figure 10-1 is a simplistic diagram of this method; it pictures a satellite in Earth orbit. The density of the model Earth is assumed to be homogeneous except for an excess mass M at some point under the orbit. As the satellite approaches M, the added gravitational force exerted by M will accelerate the satellite. As the satellite moves away from M, the corresponding retarding force will reduce the satellite velocity. By measuring the time history of the velocity variation during the period when the satellite is under the influence of M, the size, position, and magnitude of the excess mass M can be deduced. This approach was used to discover and measure lunar mascons (ref. 10-2).

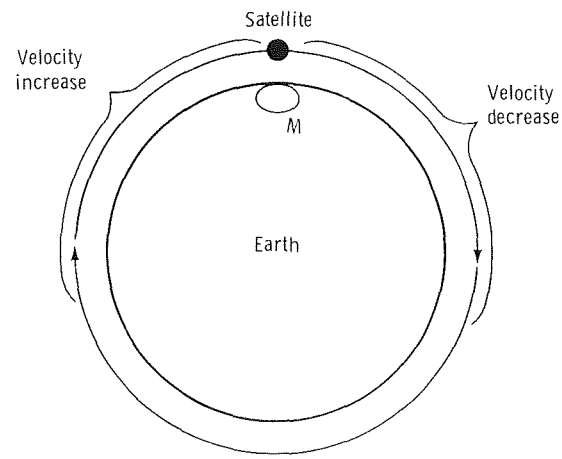

FIGURE 10-1.—Velocity changes associated with a gravity anomaly.

Of course, the actual situation for the experiment is more complex, not only because of the internal mass distribution of the Earth and its effects on the satellite trajectory, but also because the velocity of the satellite must be measured from another satellite. A detailed analysis of more realistic cases has been reported by Schwarz (ref. 10-3). Wolff (ref. 10-4), Comfort (ref. 10-5), and Vonbun (ref. 10-6) have also contributed to the investigation of this method.

From surface-gravimeter data for the United States, Schwarz constructed arrays of 1° by 1°, 2° by 2°, and 5° by 5° gravity anomalies and computed the theoretical range-rate variations that would be observed between two spacecraft in orbit over these simulated gravity fields. Orbital altitudes of 200, 300, and 700 km and satellite-to-satellite separations of 200 to 600 km were used in various combinations. Noise was added to the computed range-rate data. Schwarz then inverted the process to determine the accuracy with which the simulated gravity anomalies could be recovered from the computed, noisy, range-rate (Doppler) data.

The results of Schwarz's computer experiments are briefly summarized as follows.

1. The structure of the gravity field can be determined from measurements of the variations in range rate between two spacecraft in the same nominal orbit.

2. The lateral scale of the shortest wavelength gravity feature that can be recovered using this method is approximately equal to the orbital altitude.

3. The accuracy of the recovered gravity anomalies is approximately 0.1 mm/sec^2 (10 mgal), for an accuracy of 0.5 mm/sec (1 standard deviation) in range rate between spacecraft, where each measurement is averaged over 16 to 32 seconds.

4. The ephemerides of the two spacecraft need not be determined to high accuracy; orbital errors as large as 1000 m have little effect on the solutions.

Schwarz's computer experiments suggest rather convincingly that the ASTP Doppler Tracking Experiment should produce accurate determinations of gravity anomalies having horizontal wavelengths in the range of 300 to 1000 km over those geographic regions for which measurements are obtained. The lunar-mascon experiment confirms this conclusion even though the geometry was somewhat different because one of the "spacecraft" terminals was located on the Earth.

Useful data can be obtained when the spacecraft are within line of sight of each other, when the line between them lies above the troposphere, and when their separation is greater than 200 km. It is important to note that gravity-field information is obtained only for those particular geographic regions where the Doppler measurements are made. The scientific usefulness of the experiment thus depends on the geographic coverage.

The accelerations produced by atmospheric drag and radiation pressure on the spacecraft contribute to the measured range rates and thus constitute systematic errors in the determination of the gravity field. The acceleration caused by radiation pressure was computed for solar flux incident on the side of the spacecraft. In this case, the area-to-mass ratio is approximately 0.02 cm^2/g. The pressure exerted by direct solar radiation was taken as 4.5×10^{-10} N/cm^2 (4.5×10^{-5} dyn/cm^2); therefore, the resulting acceleration is approximately 1×10^{-6} cm/sec^2, which is negligible.

The acceleration produced by atmospheric drag a was computed for the case in which the spacecraft velocity vector is parallel to its long axis, with an effective area-to-mass ratio A/m of 0.005 cm^2/g. The following equation was used:

$$a = \frac{C_D}{2} \frac{A}{m} \rho v^2 \qquad (10\text{-}1)$$

where the drag coefficient C_D is 2, ρ is the atmospheric density, and v is the spacecraft velocity. When $\rho = 2.8 \times 10^{-13}$ g/cm^3 at an altitude of 200 km, an acceleration of 0.0084 mm/sec^2 is obtained. For the 10-second averaging time of the Doppler observations, the velocity change is thus 0.084 mm/sec for each data-sample period.

If drag accelerations are reasonably smooth, as is expected, it should be possible to separate the

gravity variations satisfactorily even at a spacecraft altitude of 200 km. Alternatively, the drag forces appear small enough that they can be modeled to sufficient accuracy. In any event, the drag effects are large enough that they must be computed accurately by using the measured orbital and altitude motions of both spacecraft.

Ionospheric Studies Using Satellite-to-Satellite Doppler Data

If a radiofrequency (RF) Doppler link is used between two spacecraft to obtain range-rate data, information about the electron concentration between the spacecraft can also be obtained. In fact, the effects of the ionosphere must be identified before accurate range rates can be determined. Consequently, a secondary goal of the Doppler Tracking Experiment was to analyze the resulting ionospheric information. In addition, it should be possible to probe traveling ionospheric disturbances with the satellite-to-satellite link and to detect the boundaries of turbulent regions of the ionosphere.

The analysis of ionospheric information is an extension of well-known methods (differential Doppler) of measuring the time change of the integrated electron concentration and other properties of the ionosphere along a radio path between a terminal moving within or above the ionosphere and a station on the ground. Before artificial-satellite flights, these techniques were used in suborbital rocket flights to measure ionospheric parameters (refs. 10-7 and 10-8). Since 1957, much information based on the use of multifrequency Doppler links between satellites and ground stations has been published (refs. 10-9 to 10-17).

A fundamental problem in space-to-ground Doppler links is that the differential Doppler shift between two coherent, harmonically related frequencies is connected to the time derivative of the columnar electron content and not to the columnar content itself. This difficulty can be removed if simultaneous measurements are made of Faraday rotation. When Faraday rotation is not observed, the problem is not adequately determined, and inversion of differential Doppler data into columnar content strongly depends on the presence of horizontal gradients in that region of the ionosphere swept through by the space-to-ground radio path while the spaceborne terminal is in motion.

The ASTP Doppler Tracking Experiment introduced a new feature, namely, measurements of horizontal gradients at a height near 220 km by use of a dual-frequency radio link between spacecraft in the same orbit.

In the case of a probe transmitting at frequency ω_1 through the ionosphere with a receiver on the ground

$$\Phi_1(t) = \frac{\omega_1}{c}\int_0^{r(t)} n_1(r)\,dr \qquad (10\text{-}2)$$

when the spacecraft is at a height $r(t)$ and where c is the velocity of light in free space and $n_1(r)$ is the index of refraction for frequency f_1 at height r. The symbol $\Phi_1(t)$ denotes the phase shift imparted at the frequency $f_1 = \omega_1/2\pi$ to the transmitted signal due to passage through the ionosphere, and its time derivative (time derivatives throughout are indicated by dots) is

$$\dot{\Phi}_1(t) = \frac{\omega_1}{c}\frac{d}{dt}\int_0^{r(t)} n_1(r)\,dr \qquad (10\text{-}3)$$

The change of phase path with time is due in part to the spacecraft motion and in part to temporal changes of the index of refraction along the vertical between the spacecraft and the ground. If there are no temporal changes in the index of refraction along the path, and if the spacecraft is assumed to be at height r_0 at time t_0, the resulting equation is

$$\dot{\Phi}_1(t_0) = \frac{\omega_1}{c}\dot{r}(t_0)\,n_1(r_0) \qquad (10\text{-}4)$$

where $\dot{r}(t_0)$ is the range rate at time t_0. If there are temporal changes, equation (10-4) becomes

$$\dot{\Phi}_1(t_0) = \frac{\omega_1}{c}\left[\dot{r}(t_0)\, n_1(r_0) + \int_0^{r(t)} \frac{\partial n_1(r)}{\partial t}\, dr\right] \tag{10-5}$$

where the term

$$\int_0^{r(t)} \frac{\partial n_1(r)}{\partial t}\, dr$$

represents the temporal variation of the columnar refractivity in the entire vertical path between the spacecraft and the ground. The problem is not adequately determined, and unless this variation is otherwise measured or becomes negligibly small, the inferring of $n_1(r_0)$ from $\dot{\Phi}_1(t_0)$ is affected by error.

When the effects of the Earth's magnetic field and the collision frequency on the index of refraction are disregarded, equation (10-4) can be rewritten as

$$\dot{\Phi}_1(t_0) = \frac{\omega_1}{c}\,\dot{r}(t_0)\left(1 - \frac{2\pi e^2 N}{m\omega_1^{\,2}}\right) \tag{10-6}$$

where N is the electron density and e and m are the charge and the mass of the electron, respectively; $2\pi\, e^2/m = 1587.6$ if N is expressed in electrons per cubic meter and if ω_1 is expressed in radians per second. From equation (10-4), the local index of refraction (and, hence, the electron density) at the spacecraft height can be determined by monitoring the received Doppler shift and by knowing, independently, the velocity of the spacecraft and the frequency radiated. With a single frequency, it is necessary to know these two parameters very accurately. However, by adding a second frequency, ω_2, the equation of the differential Doppler shift in the spacecraft-to-ground link, when temporal changes are neglected, becomes

$$\begin{aligned}\delta\dot{\Phi} &= \dot{\Phi}_1(t) - \frac{\omega_1}{\omega_2}\dot{\Phi}_2(t) \\ &= \frac{\omega_1}{c}\frac{d}{dt}\int_0^{r(t)}\left[n_1(r) - n_2(r)\right]dr \\ &= \frac{\omega_1}{c}\,\dot{r}(t_0)\left[n_1(r_0) - n_2(r_0)\right]\end{aligned} \tag{10-7}$$

where $\dot{\Phi}_2$ is the Doppler shift at frequency $f_2 = \omega_2/2\pi$ and $n_2(r)$ is the index of refraction at frequency f_2 and height r. If the refractive effects of the Earth's magnetic field and the collision frequency are disregarded, the results are

$$\delta\dot{\Phi} = \frac{\omega_1}{c}\,\dot{r}(t_0)\,\frac{2\pi e^2 N}{m}\left(\frac{\omega_1^{\,2} - \omega_2^{\,2}}{\omega_1^{\,2}\omega_2^{\,2}}\right) \tag{10-8}$$

Equation (10-8) shows that the contribution to the measurement error arising from an error in estimating the link's frequencies is virtually eliminated.

Equation (10-6) indicates that an error in frequency contributes directly to the error in $\dot{\Phi}_1(t_0)$. However, equation (10-8) shows that the error in frequency must now be multiplied by the quantity $(n^2 - 1)/\omega_1^{\,2}$, which is usually very small. For instance, if $\omega_1/\omega_2 = n = 2$ and if $\omega_1 = 2\pi \times 300 \times 10^6$ rad/sec, then $(n^2 - 1)/\omega_1^{\,2} = 8.6 \times 10^{-19}$; therefore, the influence of the frequency error in the overall error of $\dot{\Phi}_1(t_0)$ is eliminated.

When the spacecraft trajectory is not vertical, other analytical expressions, which have already been developed by several authors, must be used. However, these expressions show that the problem is inadequately determined even in the planar

approximation. The difficulty was partly alleviated in this experiment by the fact that the DM-to-CSM dual-frequency link measured the horizontal gradients in the orbital plane at the ASTP orbital height

$$\delta\dot{\Phi} = \dot{\Phi}_1(t) - \frac{\omega_1}{\omega_2}\dot{\Phi}_2(t) = \frac{\omega_1}{c}\frac{\partial}{\partial t}\left[\int_{DM}^{CSM} n_1(x)\,dx - \int_{DM}^{CSM} n_2(x)\,dx\right] \quad (10\text{-}9)$$

where x is the coordinate of the line joining the CSM and the DM. By assuming that the two spacecraft remained at a constant separation (had a relative velocity of zero), the results obtained will be

$$\delta\dot{\Phi} = \frac{\omega_1}{c}\int_{DM}^{CSM} \frac{\partial}{\partial x}\left[n_1(x) - n_2(x)\right]\frac{\partial x}{\partial t}\,dx \quad (10\text{-}10)$$

where $\partial x/\partial t$ is known from orbital-mechanics considerations. By neglecting the refractive effects of the Earth magnetic field and the collision frequency, equation (10-10) can be rewritten as follows.

$$\delta\dot{\Phi} = \frac{\omega_1}{c}\frac{2\pi e^2}{m}\left(\frac{\omega_1^2 - \omega_2^2}{\omega_1^2\omega_2^2}\right)\int_{DM}^{CSM}\frac{\partial N}{\partial x}\frac{\partial x}{\partial t}\,dx \quad (10\text{-}11)$$

The horizontal gradient of the electron content $\partial N/\partial x$ can therefore be obtained from the measured values of $\delta\dot{\Phi}$ in the DM-to-CSM path. Before it can be used in the processing of the data, however, $\partial N/\partial x$ must be known all along the vertical z. In fact, what is needed is the function

$$\int_0^z \frac{\partial N}{\partial x}\,z\,dz$$

and not just $\partial N/\partial x$ at the ASTP orbital height of 220 km. Therefore, a model must be constructed of $(\partial N/\partial x)z$ in the lower ionosphere, with the constraint of satisfying both the value measured at 220 km by the DM-to-CSM link and a value equal to zero measured at the bottom of the ionosphere. A linear variation of the gradient between these two values thus seems to be an acceptable assumption.

The investigators were unable to observe Faraday rotation (rotating Doppler) in either link. In the DM-to-CSM link, the transmitting antenna was linearly polarized and the receiving antenna was circularly polarized; and in the DM-to-ground link, there was no provision for recording signal strength.

Analysis of DM Motion About the Center of Mass

Knowledge of the orientation of the two spacecraft is required for an exact evaluation of the forces acting on their centers of mass. Atmospheric drag and radiation pressure depend on the orientation, and, in principle, the gravitational force depends to second order; but these forces are small enough that only crude orientation information is necessary. However, the observed Doppler signal measures the relative velocity of the antenna phase centers of the DM transmitter and the CSM receiver, which includes the antenna motion around the respective center of mass of these two bodies. To reconstruct the relative motion of the centers of mass, the rotational motion of the DM must be reconstructed from Doppler measurements of the relative velocity of the antenna phase center.

Whereas telemetry data were available on CSM motion (such as gyro rate and gimbal position), the only existing direct information on the orientation of the DM was obtained from the Doppler

signals and from the photographs taken from the CSM during the first 5 minutes after separation. To simulate the motion of the DM, the fundamental assumption was made that the DM is a rigid body (taken with its origin at the DM center of mass and with its axes coincident with the principal axes of the central inertia ellipsoid) subjected only to thermal expansion and contraction. With respect to a reference system, uncertainties exist in (1) the initial conditions, (2) the position of the antenna center, and (3) the geometry and orientation of the radiation pattern. In constructing the equations of motion, the investigators considered all the torques acting on the DM and selected those that had a measurable effect, namely, gravitational torque, atmospheric effects, radiation-pressure effects, and magnetic-torque effects.

As a straightforward method, the investigators chose to integrate the three Eulerian equations considered to be first-order differential equations in ω_1, ω_2, and ω_3 (components of the angular velocity with respect to the body-fixed axes), plus nine first-order auxiliary equations in the direction cosines of the body-fixed axes with respect to an inertial frame. The Eulerian equations are

$$A\dot{\omega}_1 - (B - C)\omega_2\omega_3 = T_1^*$$

$$B\dot{\omega}_2 - (C - A)\omega_3\omega_1 = T_2^*$$

$$C\dot{\omega}_3 - (A - B)\omega_1\omega_2 = T_3^* \qquad (10\text{-}12)$$

where A, B, and C are the principal moments of inertia of the DM with the ordering $A < B < C$; $\dot{\omega}_1$, $\dot{\omega}_2$, and $\dot{\omega}_3$ are the components of the angular acceleration; and T_1^*, T_2^*, and T_3^* are the components of the applied torque about the body-fixed axes x, y, and z, respectively. If **i**, **j**, and **k** are the unit vectors along the body-fixed principal axes and **I**, **J**, and **K** are the unit vectors of the inertial coordinate system, then the direction cosines α_i, β_i, and γ_i are defined as follows:

$$\mathbf{I} = \alpha_1\mathbf{i} + \alpha_2\mathbf{j} + \alpha_3\mathbf{k}$$

$$\mathbf{J} = \beta_1\mathbf{i} + \beta_2\mathbf{j} + \beta_3\mathbf{k}$$

$$\mathbf{K} = \gamma_1\mathbf{i} + \gamma_2\mathbf{j} + \gamma_3\mathbf{k} \qquad (10\text{-}13)$$

Then, since $d\mathbf{I}/dt = 0$,

$$\dot{\alpha}_1\mathbf{i} + \dot{\alpha}_1\boldsymbol{\omega} \times \mathbf{i} + \dot{\alpha}_2\mathbf{j} + \alpha_2\boldsymbol{\omega} \times \mathbf{j} + \alpha_3\mathbf{k} + \boldsymbol{\omega} \times \mathbf{k} = 0 \qquad (10\text{-}14)$$

where $\boldsymbol{\omega}$ is the angular velocity vector. Expanding the cross products, the following three scalar first-order differential equations are obtained:

$$\dot{\alpha}_1 = \alpha_2\omega_3 - \alpha_3\omega_2$$

$$\dot{\alpha}_2 = \alpha_3\omega_1 - \alpha_1\omega_3$$

$$\dot{\alpha}_3 = \alpha_1\omega_2 - \alpha_2\omega_1 \qquad (10\text{-}15)$$

The second and third parts of equations (10-13) can be differentiated to obtain similar equations for $\dot{\beta}_i$ and $\dot{\gamma}_i$.

$$\dot{\beta}_1 = \beta_2\omega_3 - \beta_3\omega_2$$

$$\dot{\beta}_2 = \beta_3\omega_1 - \beta_1\omega_3$$

$$\dot{\beta}_3 = \beta_1\omega_2 - \beta_2\omega_1 \qquad (10\text{-}16)$$

and

$$\dot{\gamma}_1 = \gamma_2\omega_3 - \gamma_3\omega_2$$

$$\dot{\gamma}_2 = \gamma_3\omega_1 - \gamma_1\omega_3$$

$$\dot{\gamma}_3 = \gamma_1\omega_2 - \gamma_2\omega_1 \qquad (10\text{-}17)$$

The set of first-order differential equations (eqs. (10-12) and (10-15) to (10-17)) can then be integrated numerically, provided that T_1^*, T_2^*, and T_3^* are suitably specified as functions of time or of ω_i, α_i, β_i, and γ_i.

To integrate the preceding equations numerically, only the gravitational torque was used. In one case, the DM was considered initially to be tumbling about its axis at a rate of 3°/sec normal to a fixed orbital plane. In another case, with the same initial conditions, the orbital plane was allowed to precess at a rate of 5.5°/day. After 4 hours, the amplitude of the modulation of ω_3 was unchanged, remaining at approximately 1.8×10^{-5} rad/sec, and the modulations of ω_1 and ω_2, although increasing secularly, were less than 5×10^{-7} rad/sec. The effects of gravitational torque are therefore negligible. The same conclusion must be applicable to the effects of the other torques considered previously.

While analyzing the data, it was found that the tumble period changed from 70.5 to 71.9 seconds; this phenomenon remains unexplained. Several possibilities were examined, but none have any observational support. Among them is the possible variation of the inertia tensor of the DM. This variation might result in part from secular effects due to an increase in mean temperature; the periodic component of the temperature change explains reasonably well the variation of the tumbling rate when the DM moved from sunlight to shadow. Other possibilities include the motion of unsecured items inside the DM that might have been subjected to the field of forces, such as centrifugal, established in the DM. These centrifugal forces, combined with the periodic thermal variation, may increase the moment of inertia about the tumbling axis and thus cause a decrease in the tumbling rate. Although some perplexity remains in this aspect of the problem, it appears from the data that the fundamental characteristics of the motion can be described accurately enough, at least in a first approximation, by assuming, as the investigators did, that the motion of the DM is that of a rigid body free of torque during properly limited intervals of time.

The results of the analysis confirm the importance of accurately reconstructing the motion of the DM about its center of mass and the shape and orientation of the antenna radiation phase pattern to remove from the raw Doppler data those components that are unrelated to the gravity field. The Doppler accuracy required implies such a detailed reconstruction that even the thermal behavior of the DM and the relative lack of rigidity of the vehicle, perhaps due to somewhat loosely clamped parts in its interior, have a substantial effect that is capable of jeopardizing the gravity experiment.

Unfortunately, the harmonic components removed from the raw Doppler spectrum were within the spectral band of the gravity-anomaly-induced signals. Therefore, their removal, although fully justified because they were attributable to the DM rotational motion, partly affected the detectability of gravity anomalies. Another peculiar occurrence, which is due to the geometry of the DM, is the fact that the precessional period of the DM is almost exactly equal to three times the tumbling period.

EQUIPMENT

Several pieces of equipment were built for the Doppler Tracking Experiment. A dual-frequency transmitter (fig. 10-2) and monopole antenna were mounted on the DM; the service module carried a receiver and signal processor (fig. 10-3) together with a circularly polarized dual-frequency antenna; in the CSM with the astronauts was a pair of small tape recorders used to store the data for postflight analysis.

Special tape-reading equipment was used during prelaunch system tests and for reading the data from the flight tapes. In the latter application,

the tape reader was controlled by, and fed data to, a standard commercial minicomputer.

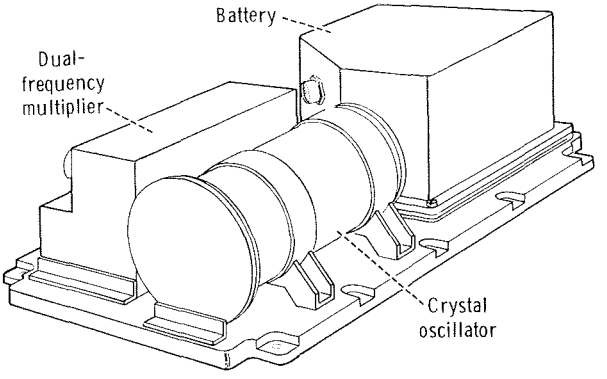

FIGURE 10-2.—The Doppler tracking transmitter.

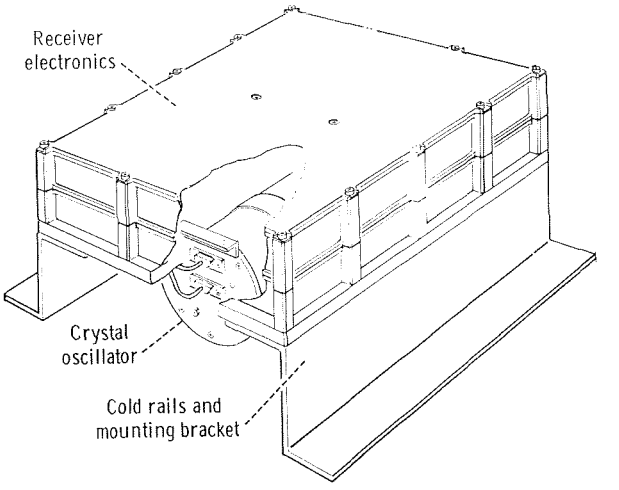

FIGURE 10-3.—The Doppler tracking receiver and signal processor.

Transmitter

The transmitter, which weighed approximately 7 kg, consisted of a highly stable crystal oscillator, frequency multipliers, amplifiers, and a diplexer. The diplexer combined the two frequencies for transmission from a single antenna. A block diagram of the transmitter is shown in figure 10-4. To save battery power for the operational phase of the experiment, the transmitter was powered directly from the spacecraft during the 50-hour warmup period required by the oscillator. The frequency of the oscillator was set for 5.06 MHz. Its excellent stability (1.5 parts in 10^{12} over both 10- and 100-second averaging intervals) was preserved by carefully insulating it from environmental changes over a temperature range of 255 to 311 K (0° to 100° F). A single multiplier chain

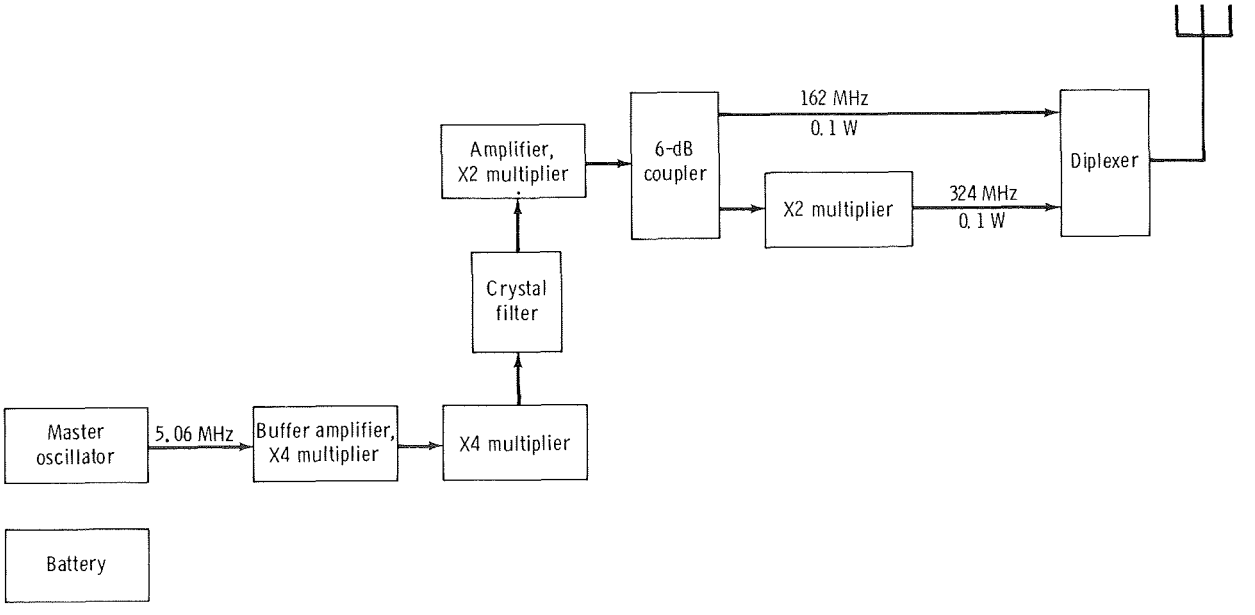

FIGURE 10-4.—Block diagram of the transmitter.

multiplied, amplified, and filtered the oscillator output and drove a power divider. One of the power-divider outputs drove the 162-MHz input of a diplexer; the second was frequency-doubled and was used to feed the 324-MHz diplexer input. The diplexer provided input isolation and filtering. At least 100 mW of output power was delivered to the dual-frequency antenna at each of the two frequencies.

Receiver and Signal Processor

The receiver, which also weighed approximately 7 kg, is shown in block diagram form in figure 10-5. It provided the processor with a Doppler output compatible with transistor-to-transistor logic for each input frequency. The frequency and phase variations of the 162- and 324-MHz inputs were retained through the use of second-order phase-lock loops. Thus, the receiver outputs were actually band-pass-filtered and constant-amplitude replicas of the input signals, translated from 162 and 324 MHz to 1 kHz. The choice of 1 kHz as the center frequency for the processor represented a compromise between a desire for high accuracy (requiring a low frequency) and the need to avoid the ambiguity that could result if the Doppler signal shifted this frequency negatively by more than 1 kHz. Because the maximum anticipated Doppler shift was approximately 350 Hz, a 1-kHz center frequency left an adequate margin without significantly degrading the attainable measurement accuracies.

The receiver was powered internally by means of dc-to-dc converters, regulators, and filter circuitry. Less than 50 W of spacecraft power was needed to operate both the receiver and the tape recorder.

Both the transmitting and the receiving antennas were dual-frequency units. The former was a vertical monopole that acted as a quarter-wave antenna at frequencies of 162 and 324 MHz. At 324 MHz, an inductor near the midpoint of the antenna isolated the top section from the bottom; at 162 MHz, the inductor acted as a small loading coil. The receiving antenna was approximately 1 m square and contoured to fit against the side of the service module. This antenna was a strip-line conformal array in which tuned stubs were used to couple its sections at 162 MHz and to isolate the sections at 324 MHz.

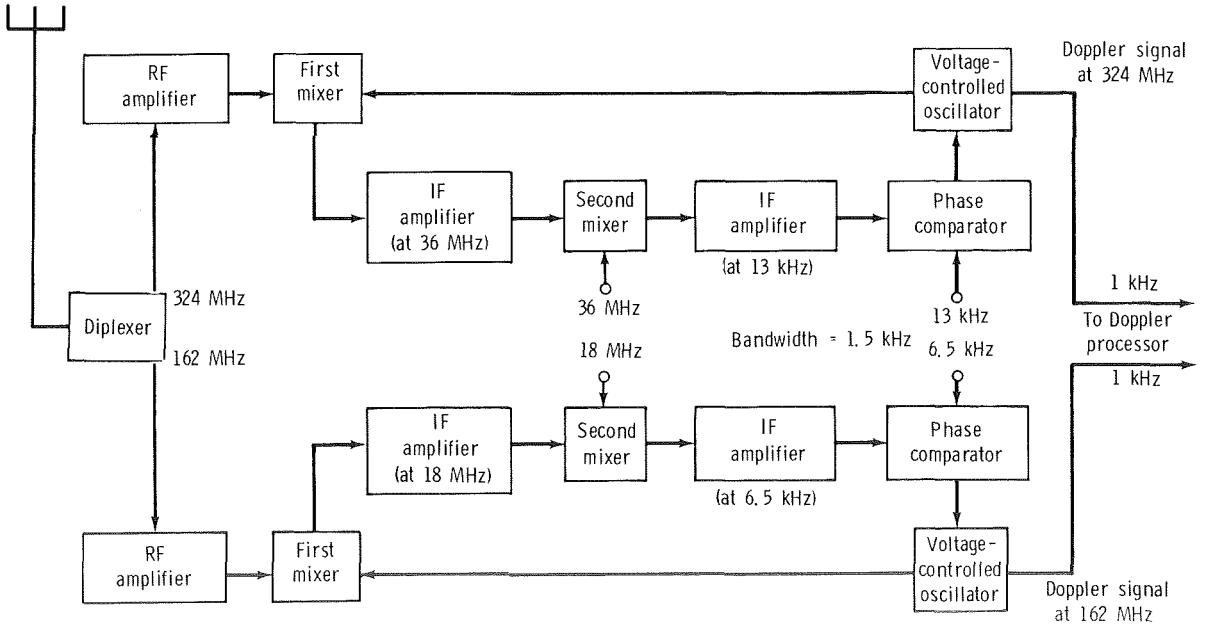

FIGURE 10-5.—Block diagram of the receiver.

A 5.0-MHz reference-frequency input to the synthesizer and the timing reference for the Doppler processor were supplied by an oscillator that was identical, except for its frequency, to that in the transmitter. The synthesizer (having output frequencies, derived by frequency multiplication and division, that were phase coherent with the reference) provided all local-oscillator injections and phase-detector references. When required, band-pass filters were used to obtain outputs of sufficient spectral purity.

A diplexer at the receiver input divided the single input from the dual-frequency antenna into two channels. A preamplifier and a mixer followed the diplexer. These stages had a noise figure of less than 8 dB and a first intermediate-frequency (IF) image-rejection capability of greater than 60 dB. For each channel, a second IF image-rejection capability of at least 60 dB was achieved by means of a crystal filter. The first IF amplifier included two automatic-gain-controlled stages, and the second included four active filters with amplitude limiting at each stage. The second IF amplifier was followed by sine and cosine phase detectors and filters; the first developed the loop filter voltage fed to the voltage-controlled oscillator (VCO), and the second provided both the automatic-gain-control voltage for the first IF amplifier and a lock/out-of-lock signal to the Doppler processor. The VCO module output fed to the first mixer was derived by multiplying and filtering the output of a crystal VCO having a frequency of 22.5 MHz.

When an out-of-lock signal was received, the processor responded by supplying the phase-detector module with one signal to change the

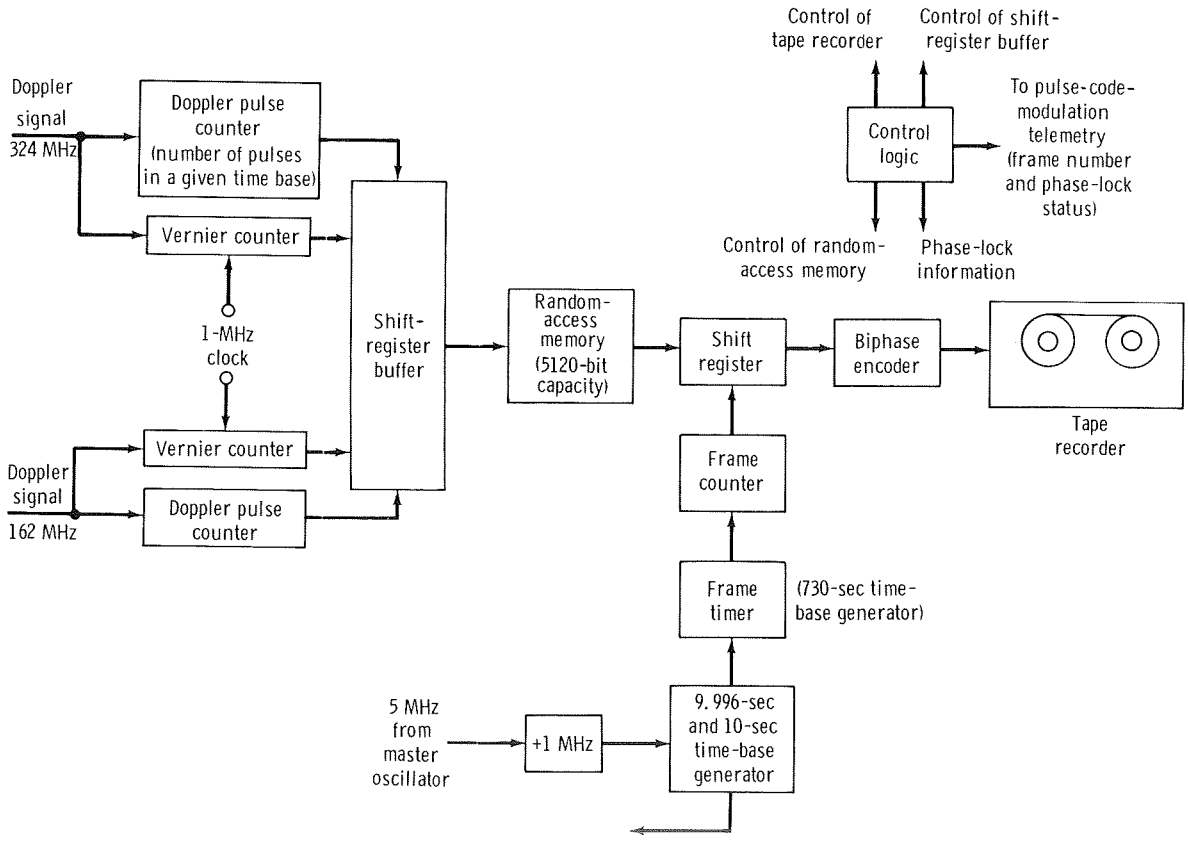

FIGURE 10-6.—Block diagram of the Doppler processor.

phase-lock-loop bandwidth from 5 to 100 Hz and another signal to inject a sweep voltage into the loop. The difference between the sweep (±5 and ±2.5 kHz at 324 and 162 MHz, respectively) and the expected Doppler shift allowed for changes in the central-voltage-to-frequency transfer characteristics of the oscillator. When lock was acquired, the signal voltages changed state, the sweeping voltage was removed, and the loop bandwidth was restored to 5 Hz.

The processor received Doppler frequency information from the receiver, extracted the desired information, and recorded and stored this information simultaneously on two tape recorders in the CSM (fig. 10-6). The Doppler frequency averaging interval counted by the processor is shown in figure 10-7. A 10-second counter identified the time instants t_0, $t_2 = t_0 + 9.996$ seconds, $t_0' = t_0 + 10$ seconds, $t_2' = t_2 + 10$ seconds, etc. The points t_1 and t_3 were determined by the first positive-going zero crossing that occurred after times t_0 and t_2, respectively. For each channel, an associated vernier up/down counter was enabled at time t_0 and counted the number of 1-microsecond clock pulses observed before it was disabled at time t_1. It was enabled again at time t_2, when it down-counted the number of clock pulses in the interval $t_2 - t_3$. Simultaneously, zero-crossing counters counted the number of positive-going zero crossings in the interval $t_0 - t_2$ for each channel. These time counts and zero-crossing counts constituted the raw data associated with each observation interval. The counters were reset and the entire process was restarted at time t_0'.

The average frequency $\hat{f}$ observed during a processor cycle was determined from these tape-recorded data by dividing the number of zero crossings Z by the observation time:

$$\hat{f} = \frac{Z}{9.996 - \Delta t} \tag{10-18}$$

where Δt represents the contents of the vernier counter. Because the zero-crossing counters and the vernier counters were 15 and 13 bits wide, respectively, an unambiguous measurement of any Doppler frequency shift less than or equal to ±750 Hz was ensured.

The Doppler processor also performed other functions. For example, it monitored lock/out-of-lock signals from the receiver; when an out-of-lock condition occurred, the processor reestablished lock status and loaded out-of-lock data into a format that could be detected during subsequent data reductions. In addition, the Doppler processor supplied high-channel phase-lock status information to the astronauts by means of a panel meter, as well as that information together with frame numbers to the telemetry channel. From this phase-lock status information, spacecraft maneuvers could have been performed to regain high-channel lock if required. (It was assumed that a high-frequency-channel lock implied a low-frequency lock because of the higher signal-to-noise ratio on the low-frequency channel.) From the telemetered frame number, the

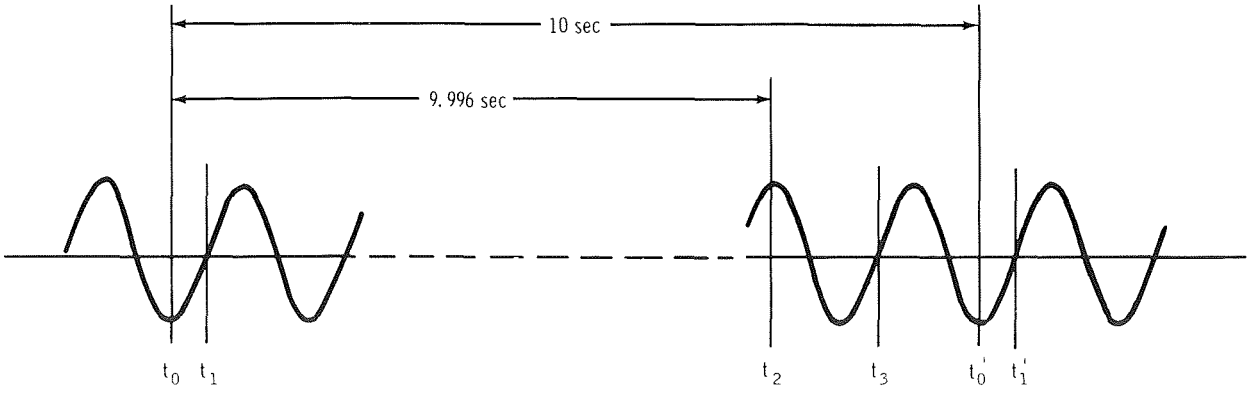

FIGURE 10-7.—Counting interval of the Doppler processor.

tape-recorded data were correlated with the position of the CSM/DM pair relative to the Earth. In another function, data on pitch, roll, and yaw rates of the CSM were received and recorded by the processor to enable the effect of the CSM motion on the Doppler shift to be compensated for during data reduction. Finally, 7-bit parity words were generated by the processor as a protection against substitution and synchronization errors.

Every 10 seconds, a data word was formatted by means of a random-access memory, shift registers, a frame counter, and a microprogramed controller. This data word consisted of the number of zero crossings and the Δt values for both low- and high-frequency channels, plus information on roll, pitch, and yaw rates and parity. After 73 words were stored as a frame, the frame number was appended and the data were serially transferred to the tape recorders at a 972-Hz bit rate through a biphase encoder. Recording time required was approximately 5.2 sec/frame.

Testing

The system was tested for oscillator stability and low noise before flight by observing the 10-second integrated-frequency measurements produced by the signal processor. The interval during flight between experiment activation and DM jettison also provided a measurement of system performance. On the ground or when the two spacecraft were docked during flight, neither Doppler shift nor ionospheric effects are possible. Thus, the time variation in the sequence of frequency measurements at each frequency indicated the stability of the transmitter oscillator relative to that of the receiver oscillator. The difference between simultaneous 324- and 162-MHz observations tested the balance of the circuitry.

Table 10-I gives the root-mean-square (rms) scatter among a small sample of data points observed at factory acceptance testing, at the NASA John F. Kennedy Space Center before the equipment was installed, on the launch pad, and in orbit. In the first two tests, the backup transmitter was used; the flight system noise in the pad test was attributed to the fact that insufficient time had been allowed for stabilization of the oscillator temperature-controlled crystals.

TABLE 10-I.—Root-Mean-Square Scatter During Testing

Test	*Scatter, mm/sec, at —*	
	162 MHz	*324 MHz*
Acceptance	4.2	0.9
Preinstallation	1.0	1.2
Pad	3.7	3.5
Orbit	1.8	1.8

The rms calculated for the entire "orbit" data set differs somewhat from the tabulated value since it includes longer term fluctuations and the frequency shift induced by g-loading the crystals when the CSM and the DM were rotated at 5°/sec just before separation. The rms difference between channels during this time (based on a small sample) was 1.4 mHz.

DATA

The Doppler Tracking Experiment had three prime sources of data: spacecraft-to-spacecraft Doppler data and related information recorded in the command module; ground tracking data from the NASA unified S-band (USB) network, from the Defense Mapping Agency Tranet Doppler tracking network, and from a number of geoceivers coordinated by the Applied Physics Laboratory; and telemetry from the CSM showing the start of each data frame and a receiver-lock indicator. These sources are described in more detail in the following subsections.

In addition, the astronauts photographed the DM shortly after it was jettisoned from the CSM. The film, which contained approximately 390 images of the DM taken at approximately 0.5-second intervals, was used to make a first estimate of the DM rotational motion.

Tape-Recorded Data

The data recorded onboard the CSM were arranged in groups called words (73 words constituted a frame). The first 8 bits in each frame gave its number, a sequential count that started when the receiver was turned on. The 73 data words followed the frame number; the first word was 87 bits long, and the rest were 69. All data groups appeared with the least significant bit first, except for the frame number, which, for reader synchronization, had its most significant bit first, thereby ensuring 127 frames (nearly 26 hours of observing time) wherein the first bit was zero.

In a Manchester biphase code generated by the signal processor, the data were to have been recorded in the CSM on a parallel pair of tape recorders. One recorder failed to run; postmission investigation revealed that the tape had become stuck to one of the heads. Fortunately, the other tape contained signals of high quality. There were no parity errors and no dropouts.

In all, 109 frames were recorded. Frame 0 contained no useful information and was generated by the signal processor only to ensure that the various registers were correctly set for the start of frame 1. Frames 1 to 15 contained data taken while the CSM and the DM were docked and constituted the final test of the equipment. Frames 16 to 41 included the period during which the CSM was maneuvered to attain a position approximately 300 km from the DM. The observational data began with frame 42, which started at 01:01:56 UT on July 24, 1975 (204:41:56 ground elapsed time), shortly after the start of orbital revolution 126. Since the receiver was turned off during frame 109, which was therefore not recorded, the data ended with frame 108, completed at 14:37:06 UT on July 24.

The Doppler measurements were continuous except for two gaps due to loss of receiver lock. One gap occurred in frames 59 to 61, and the other in frames 101 to 103.

Ground-Based Observations

The CSM was tracked by the NASA USB network, consisting of 18 stations. Eleven USB stations reported a total of 1754 observations made during 15 passes between 00:43:00 and 15:50:00 UT; 832 observations that were made at low elevation angles were rejected. The limit for range measurements was 5°; for range differences, 8°.

The DM was observed by 19 Tranet stations and 13 geoceiver stations. Between 00:00:00 and 24:00:00 UT, 216 geoceiver observations were recorded on 46 passes and 928 Tranet observations from 64 passes. From these 1144 observations, 492 were rejected because of elevation angles less than 8°.

Telemetry Data

For all times when the CSM was within range of a receiving station, the telemetry stream included a signal from the receiver indicating whether or not it was locked onto an incoming signal. Every 12 minutes 10 seconds, the start of a new frame and its number were indicated. These data, recorded on strip charts together with time signals generated at the NASA Lyndon B. Johnson Space Center, formed the basis for correlating Doppler data and spacecraft position.

DATA REDUCTION

The data-processing phase consisted of a series of computerized steps to remove from the raw data a number of corrupting effects, leaving only random system noise and the "signatures" of gravity anomalies. Both theoretical models and filtering techniques were applied. The procedure involved four basic operations: (1) point-by-point calculation and removal of the ionospheric propagation effects, (2) separate determinations of the CSM and DM orbits so that a predicted range difference could be computed for each data point, thereby taking into account all orbital effects including gravitational perturbations (except small-scale anomalies), (3) point-by-point subtraction of the calculated range differences from the observations, and (4) reduction of the rms scatter of the residuals by calculating and subtracting the com-

ponents arising from rotational motions of the spacecraft.

The ionospheric-correction technique, which is described fully in references 10-18 and 10-19, is simply the classical two-frequency correction that includes the frequency-dependent phase shift imposed by the ionosphere. Figure 10-8 is a sample of the raw data as recorded onboard the CSM; figure 10-9 shows the differential Doppler signal due to the ionosphere. Removal of the ionospheric contributions left the data, as shown in figure 10-10, with periodic excursions as large as 3 m/sec.

Orbit Determination

To suppress the large-scale variations shown in figure 10-10, a range difference was calculated for each data point from high-precision orbits of the DM and the CSM and subtracted from the observed values. The orbits were determined independently by directly integrating the equations of motion for each spacecraft and differentially correcting the initial conditions to optimize the fit to ground-based observations (Tranet Doppler observations of the DM and USB radar range and range-rate observations of the CSM).

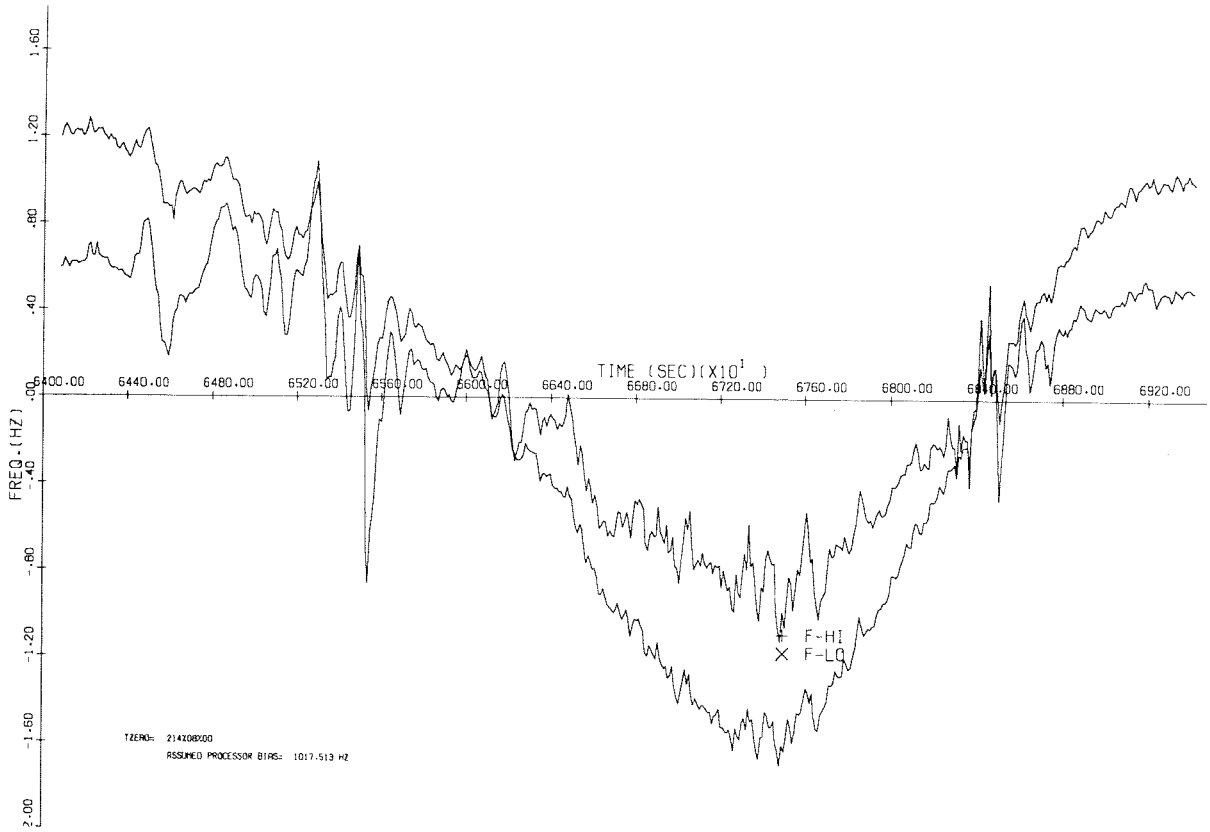

FIGURE 10-8.—Raw Doppler data as recorded onboard the CSM.

The SAO primary orbit-determination program was used to compute approximate orbits, which formed the basis for the starting set of initial conditions. To determine an appropriate set of initial conditions, it was first necessary to eliminate pass-bias errors due to oscillator uncertainties from the observed Tranet range-difference data. This procedure was accomplished by means of a series of orbit determinations within consecutive overlapping time intervals of 0.4 day spanning a total period of 2 days from modified Julian day (MJD) 42616.0 to 42618.2. To calculate the apparent frequency drift of the oscillator, a regression line was subsequently fitted to this set of biases. The slope of the regression line was found to indicate a frequency drift in 1 day of 0.417 Hz per 300 MHz, whereas the mean offset was found to be 18.4 Hz per 300 MHz. After the biases were determined, each Tranet observation was corrected and the resulting set of data was used as input to the precision orbital integration package.

An additional parameter estimated from the set of 0.4-day arcs was the DM area-to-mass ratio A/m. For a circular orbit (ref. 10-20), A/m is given

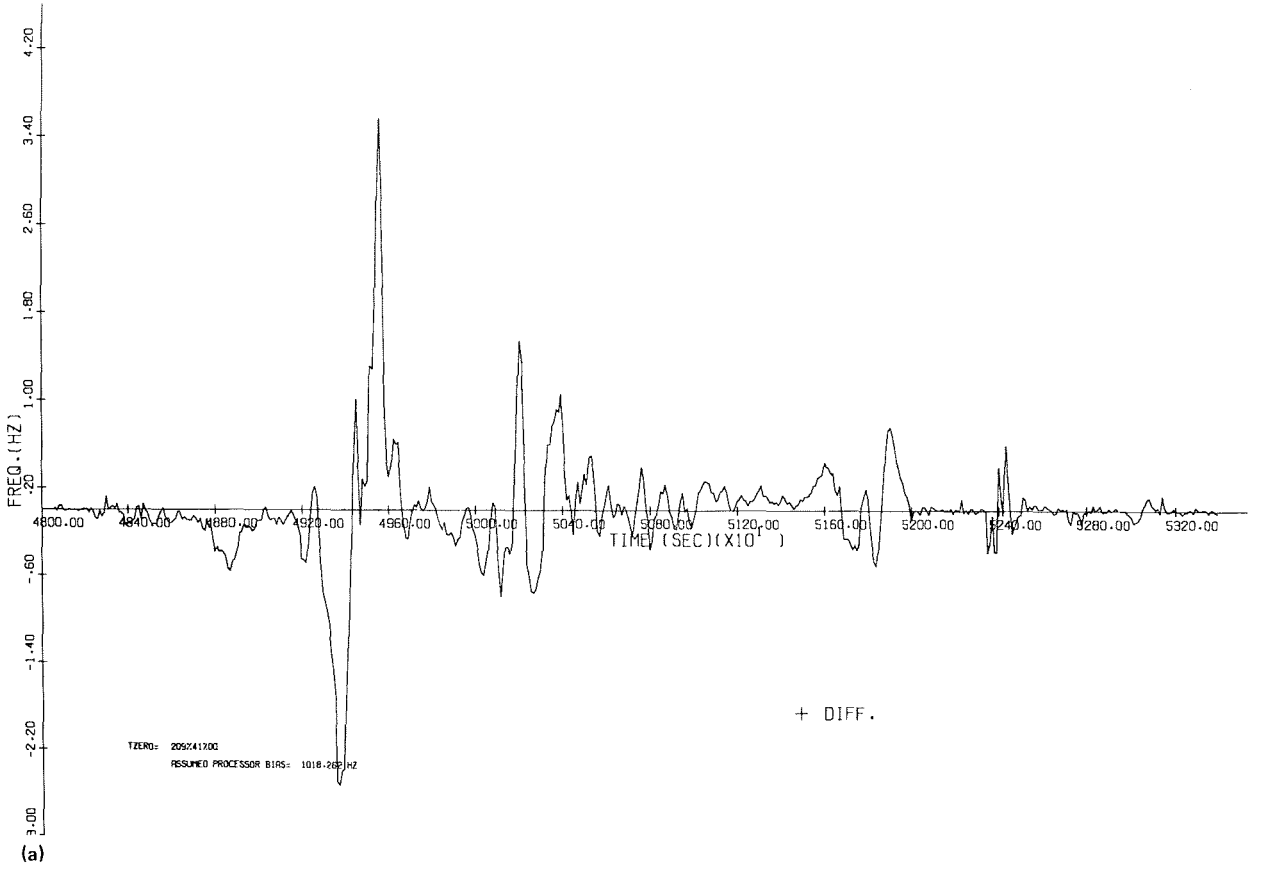

FIGURE 10-9.—Differential Doppler shift due to the ionosphere for four consecutive orbital revolutions. (a) Revolution 129. (b) Revolution 130. (c) Revolution 131. (d) Revolution 132.

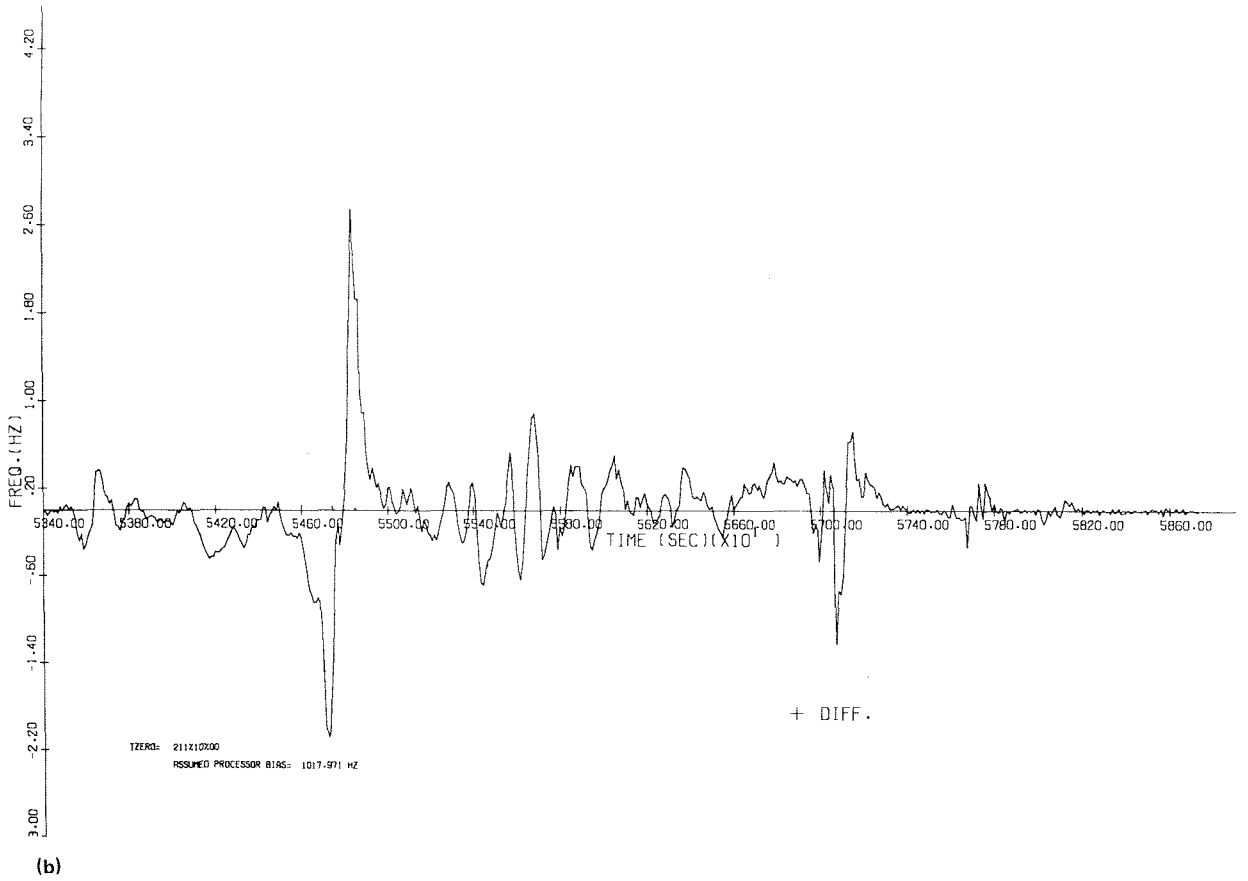

FIGURE 10-9.—Continued.

by

$$\frac{A}{m} = \frac{\dot{P}}{3\pi a \rho C_D} \tag{10-19}$$

where $\dot{P}$ is the rate of change of the orbital period, a is the semimajor axis, ρ is the atmospheric density, and C_D is the drag coefficient. Since the computer program provides the first and second time derivatives of the mean anomaly M, the value of $\dot{P}$ was obtained from

$$\dot{P} = -\frac{\ddot{M}}{2\dot{M}} \tag{10-20}$$

By assuming $C_D = 2.0$, $\rho = 10^{-13}$ g/cm^3, $a = 6.587 \times 10^8$ cm, $\dot{M} = 16.237$ rev/day, and $\ddot{M} = 9.932 \times 10^{-3}$ rev/day/day, an area-to-mass ratio for the DM of 0.030 cm^2/g was derived.

Once the pass biases, the area-to-mass ratio, and the orbital elements had all been estimated from the orbital processor, the final orbit determinations were performed by means of a precision numerical-integration package. This package consisted of a core integrator program of the Adams-Moulton type developed at the NASA Jet Propulsion Laboratory; step size and integration order were automatically chosen according to the desired accuracy. The gravity field, which was obtained from reference 10-21, included spherical-harmonic coefficients through degree and order 12. To compute lunisolar forces, positions of the

Sun and Moon were derived from reference 10-22.

Atmospheric drag D was given by (ref. 10-20)

$$D = \frac{dv^2}{2}\frac{A}{m}C_D \qquad (10\text{-}21)$$

where v is the velocity of the satellite and $C_D = 2$. The atmospheric density variation over the orbit was represented by a polynomial in time fitted with 1 percent accuracy to 500 points/rev along the nominal trajectory. The densities of these 500 points were calculated from Jacchia's static-diffusion model 39H.

Because an accurate area-to-mass ratio was not known for either satellite, the value of A/m selected was the one that minimized the standard error of the calculated orbit. Starting with an estimate of 0.030 from the orbit-computation program, the investigators varied the value of A/m for the DM from 0.01 to 0.06. The standard error of the DM orbit had a minimum value of approximately 10 m for $A/m = 0.035$ cm^2/g. The CSM area-to-mass ratio was taken as 0.002 cm^2/g, and varying it had little effect. The mean elements for the DM and the CSM are given in table 10-II. Orbits for the DM were calculated every 0.2 day, and the orbital elements are plotted in figure 10-11. Table 10-III contains the initial conditions used in the numerical-integration program.

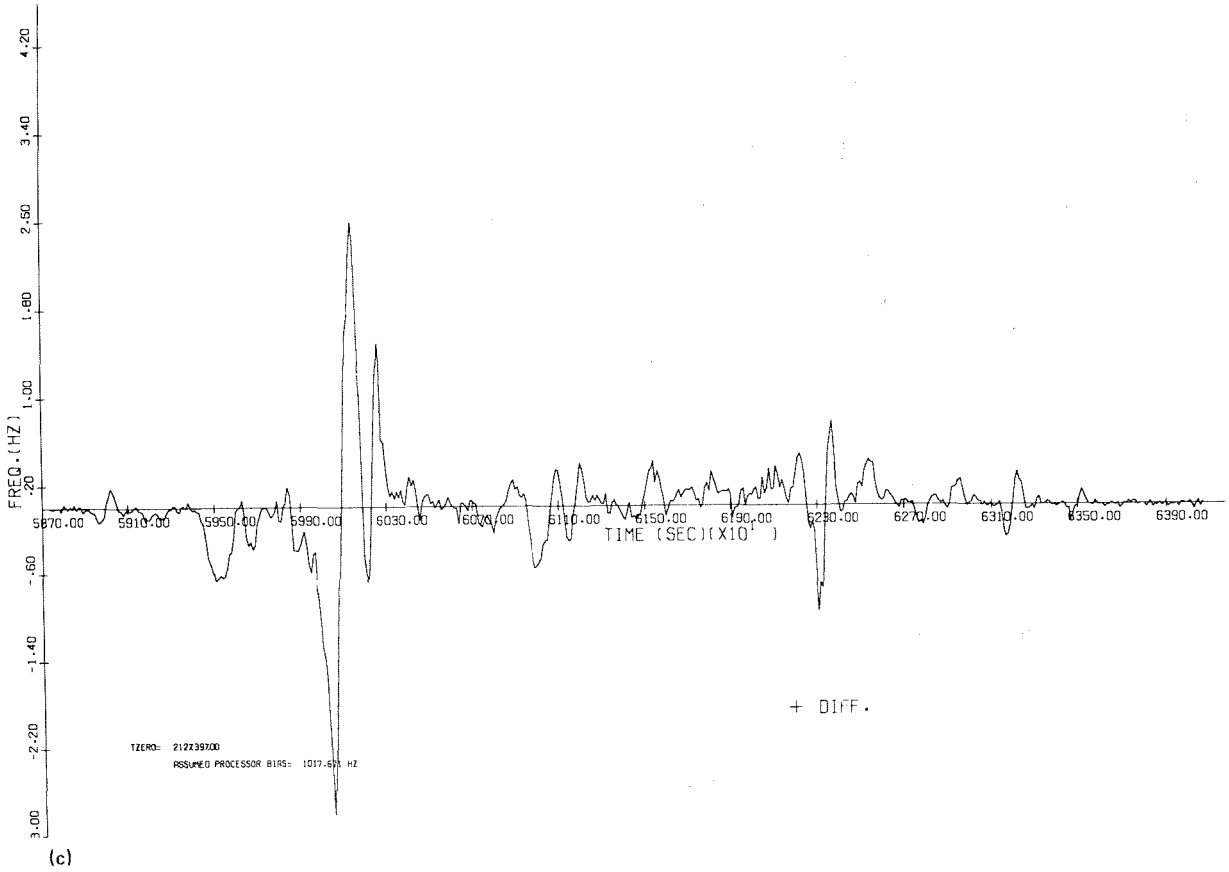

(c)

FIGURE 10-9.—Continued.

TABLE 10-II.—Instantaneous Elements for the DM and the CSM

[*Epoch = 42617.008305567 MJD*]

Element	*DM*	*CSM*
X, cm	3.369937×10^{8}	3.478627×10^{8}
Y, cm	4.567079×10^{8}	4.345419×10^{8}
Z, cm	-3.352690×10^{8}	-3.531287×10^{8}
$\dot{X}$, cm/sec	-2.859357×10^{5}	-2.672850×10^{5}
$\dot{Y}$, cm/sec	5.536761×10^{5}	5.779922×10^{5}
$\dot{Z}$, cm/sec	4.650151×10^{5}	4.461675×10^{5}

TABLE 10-III.—Orbital Data for the DM and the CSM

[*Epoch = 42617.008305567 MJD*]

Orbital element	*DM*	*CSM*
Semimajor axis, km	6590.818	6590.843
Eccentricity	0.001194	0.001237
Inclination, deg	51.7704	51.7657
True anomaly, deg	98.984865652	97.558757298
Longitude of ascending node, deg	81.3086	81.3114
Argument of perigee, deg	220.5304	219.3008

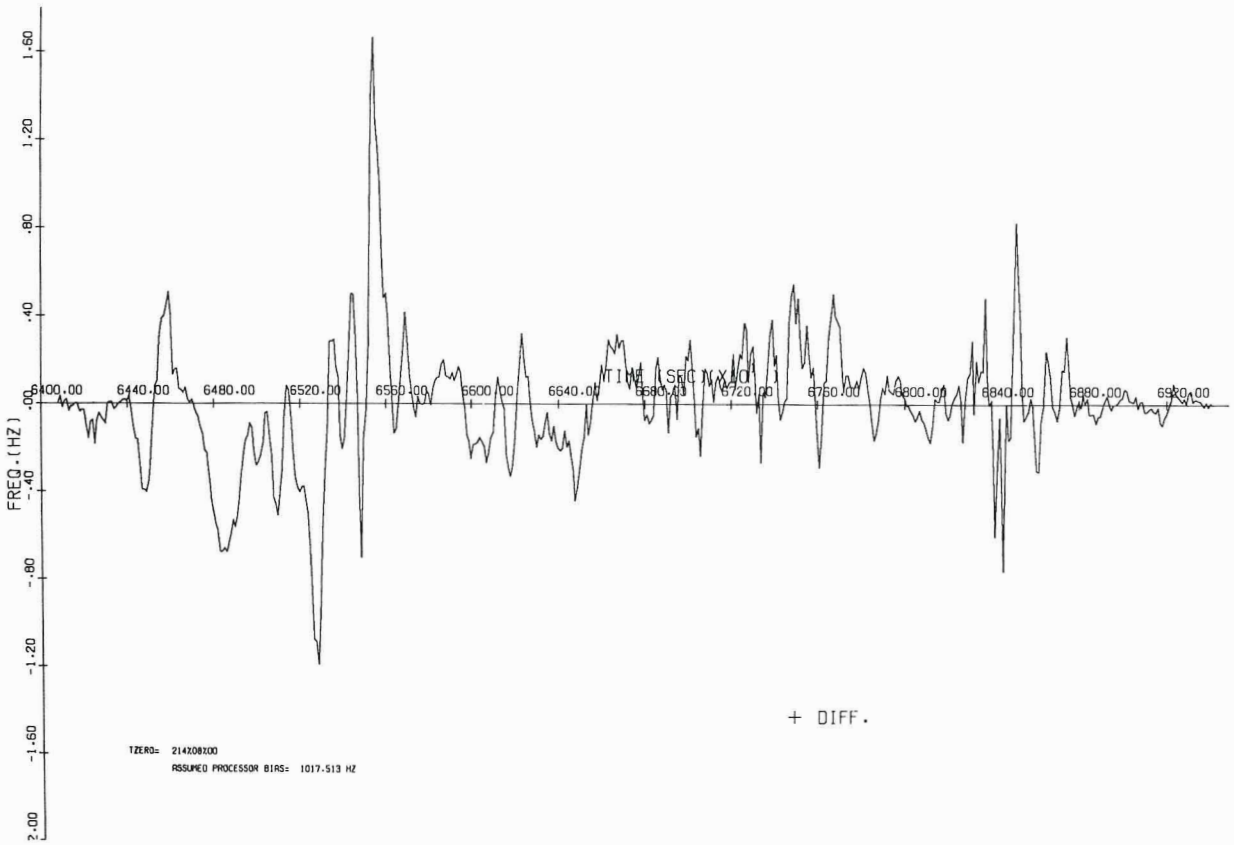

FIGURE 10-9.—Concluded.

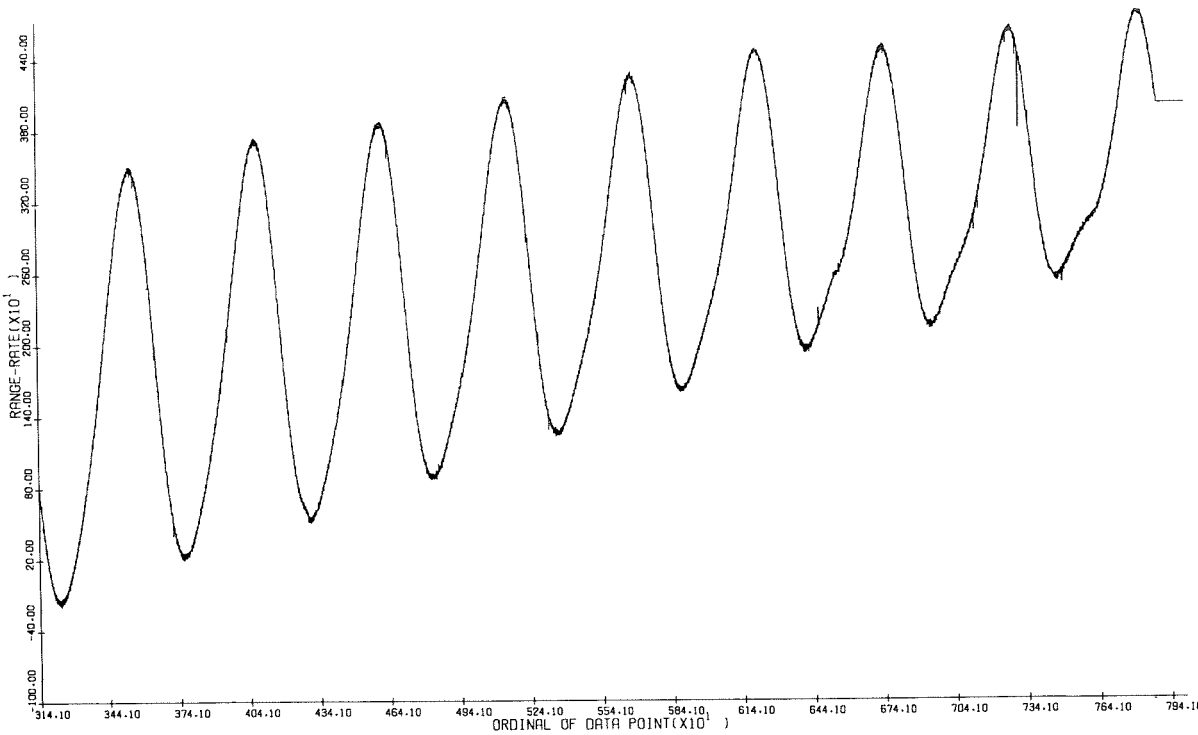

FIGURE 10-10.—Doppler data after removal of ionospheric contribution showing large-scale variations.

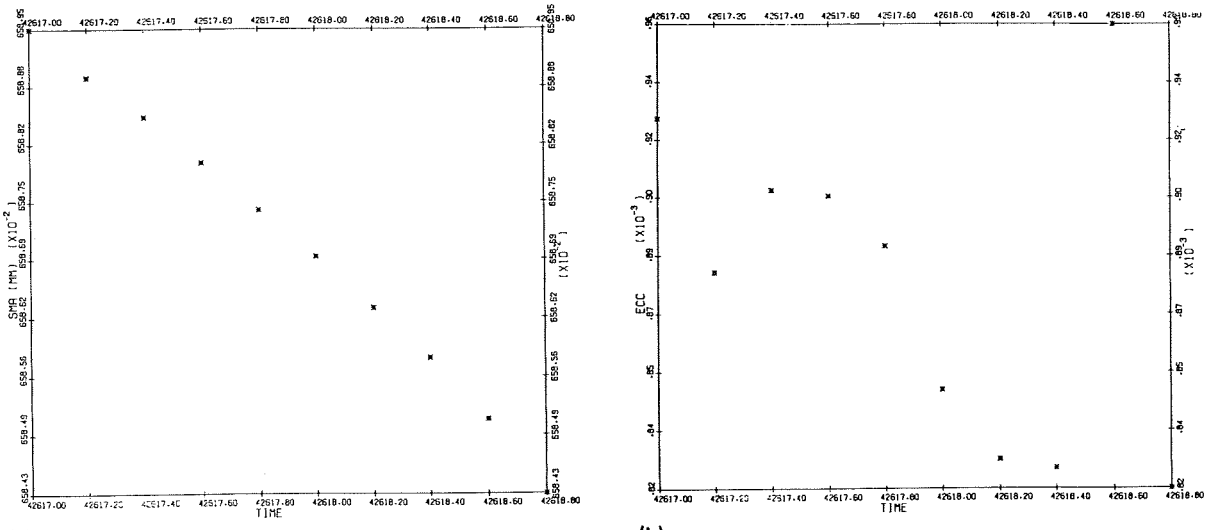

(a) (b)

FIGURE 10-11.—Mean orbital elements for the DM plotted every 0.2 day. Times are modified Julian days. (a) Semimajor axis. (b) Eccentricity. (c) Inclination. (d) Longitude of ascending node. (e) Argument of perigee.

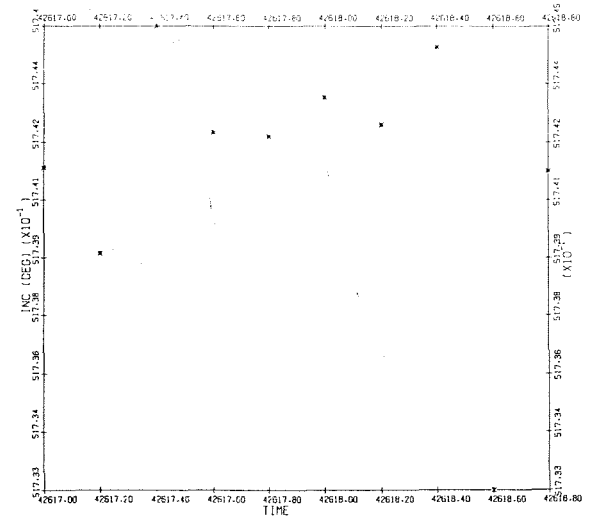

(c)

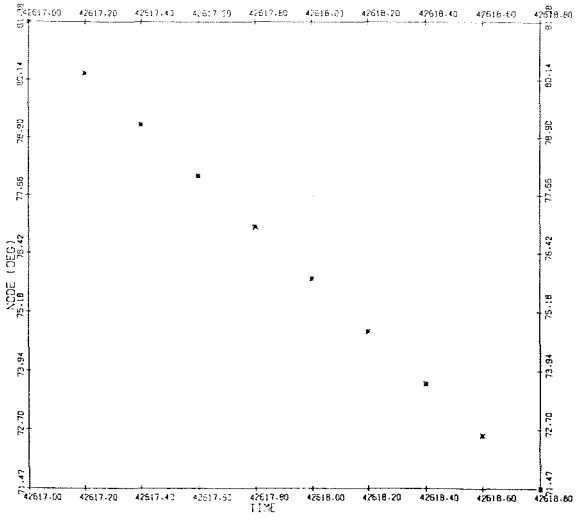

(d)

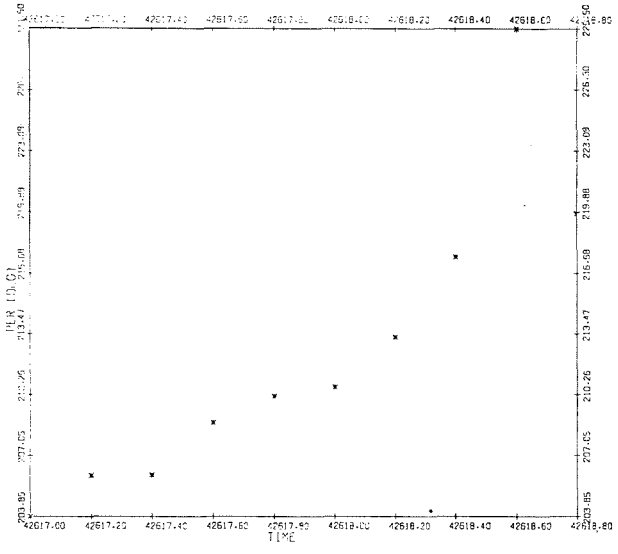

(e)

FIGURE 10-11—Concluded.

Comparison of Calculated and Observed Range Differences

Once the initial conditions were established, an ephemeris for each spacecraft was calculated. This ephemeris was the basis from which a predicted DM/CSM "Doppler signal" was computed for every 10-second interval throughout the lifetime of the experiment. When these calculated range differences were subtracted from the observations (which had been corrected for ionospheric effects), the residuals varied over a range of several hundred millimeters per second.

The range-rate residual scatter was further reduced by fitting the calculated values of $\dot{\rho}_c$ to the observed values of $\dot{\rho}_o$. By using the polynomial

$$\tilde{\dot{\rho}} = \sum_{i=1}^{15} A_i \left(t\right)^{\ell_i} \left(\dot{\rho}_c\right)^{m_i} + B \cos \frac{2\pi t}{5000} + C \cos \frac{2\pi t}{2500} \qquad (10\text{-}22)$$

where $2\pi t$ is the orbital period and the values of exponents ℓ_i and m_i ranged from 1 to 4, and where A_i, B, and C were determined in an iterative manner by means of a least-squares estimator. This process was repeated eight times, by using $\tilde{\dot{\rho}}_c$ as a new value for $\dot{\rho}_c$ each time, to reduce the scatter in the observed residuals minus the computed residuals to 20 mm/sec. The "corrections" Δv added to the range rate $\dot{\rho}_c$ calculated from the two orbits were then subjected to a Fourier analysis to ensure that the estimator had suppressed only the orbital component of the intervehicular range rate and had not introduced any "high-frequency"

components (wavelengths shorter than approximately 1000 seconds) that might be mistaken for gravity anomalies.

Determination of CSM and DM Rotation

A significant contribution to the residual scatter arises from the fact that the observed range differences were from antenna to antenna, whereas the calculated differences were between the centers of mass of the CSM and the DM. Therefore, the next step was to model the motions of the antennas relative to the centers of mass so that their effects could be removed from the residuals.

Because the receiving antenna was so nearly on the line between the centers of mass of the two spacecraft, CSM rotational motions greater than 0.1°/sec over 10-second intervals would be required to generate Doppler signals of 1 mm/sec. Fourier spectra of the rate-gyro data were examined together with the data. Since no evidence of motions approaching 0.1°/sec was found (except when the CSM was maneuvered to reacquire Applications Technology Satellite 6 after the astronauts' sleep period), no further effort was devoted to modeling CSM motions.

The DM signature was determined by finding the periods of the dynamical motion for individual segments of the data-take interval. Segmentation boundaries were closed on the times of entry into and exit from the Sun-Earth shadow. A nonlinear least-squares polynomial processor was developed and employed to determine the amplitudes, periods, and phases of the rotational range-rate components. The form of the polynomial was

$$\begin{aligned}\dot{\rho} = {} & A_1 \cos\frac{2\pi t}{P+p} + A_2 \cos\frac{2\pi t}{P-p} + \dot{A}_3 \cos\frac{2\pi t}{P} \\ & + A_4 \cos\frac{2\pi t}{\frac{P}{2}} + A_5 \cos\frac{2\pi t}{\frac{P}{3}} + A_1 \sin\frac{2\pi t}{P+p} \\ & + A_2 \sin\frac{2\pi t}{P-p} + A_3 \sin\frac{2\pi t}{P} + A_4 \sin\frac{2\pi t}{\frac{P}{2}} \\ & + A_5 \sin\frac{2\pi t}{\frac{P}{3}} \end{aligned} \tag{10-23}$$

where P is the period of rotation and p is the period of nutation, or coning. The DM rotational period was close to 72 seconds, but both periods increased with time. By assuming a linear increase, $\dot{\rho}_{DM}$ was calculated for each data point and removed from the residuals. These steps reduced the scatter by a factor of 2.

Finally, the baseline was flattened by a 40-point averaging technique, and a filter to remove periods shorter than 50 seconds was applied. By this means, residuals were reduced to an rms amplitude of 6.5 mm/sec.

A sample of the reduced data is shown in figure 10-12. A Fourier spectrum of the entire data run is shown in figure 10-13. Times of the data take and other information are given in table 10-IV.

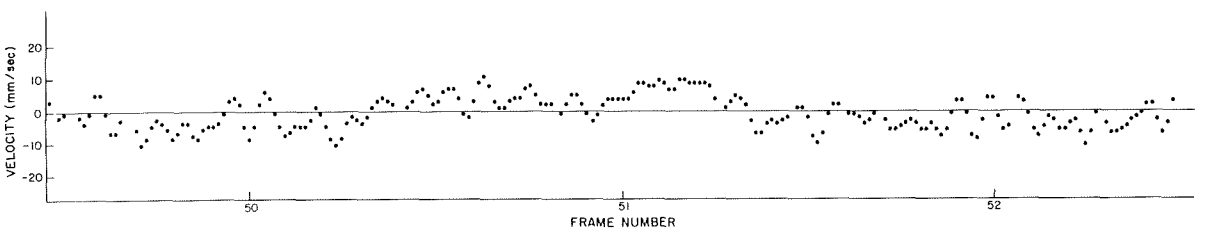

FIGURE 10-12.—Sample of reduced Doppler data. The ordinate is the relative velocity between spacecraft during revolution 126.

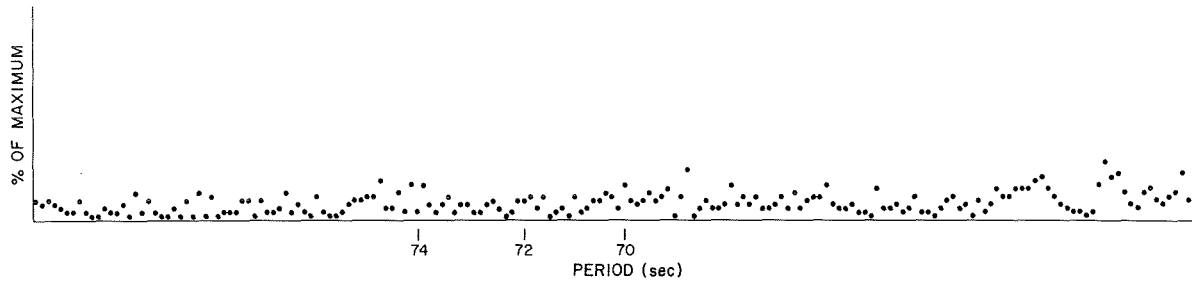

FIGURE 10-13.—Fourier spectrum of reduced Doppler data.

TABLE 10-IV.—Times of Data Take
[*July 24, 1975*]

Revolution number	*Revolution start time, UT, hr:min*	*Frame/word at meridian crossing*
126	00:56	47/31
127	02:34	54/50
128	04:12	61/69
129	05:47	69/15
130	07:20	76/34
131	08:52	83/56
132	10:24	91/03
133	11:58	98/22
134	13:34	105/41

RESULTS

The results of this rather involved analysis are discussed in two main parts. The first refers to the ionospheric observations, highly successful though not completely analyzed. The second part describes the inconclusive search for gravity signatures in the satellite-to-satellite velocity data.

The experiment design anticipated a signal-to-noise ratio near 1. With data from other sources — the Goddard Geodynamics Experiment (MA-128), surface-gravity measurements, or GEOS-3 altimetry, for example — or with a longer data take, unambiguous identificaton of gravitationally induced velocity variations would be possible and, thereby, the feasibility of this technique could be demonstrated. Unfortunately, noise levels more than twice the value expected precluded such positive identifications.

Early Results From the Ionospheric Experiment

Differential Doppler data were collected in both DM-to-CSM and DM-to-Earth paths by using the links shown schematically in figure 10-14. The goals of the ionospheric experiment were as follows (refs. 10-18, 10-19, 10-23, and 20-24):

1. To measure the time changes of the columnar electron content between the two spacecraft, from which horizontal gradients of electron density at the height of 220 km (along the orbital path of the CM/CSM pair) could be derived.

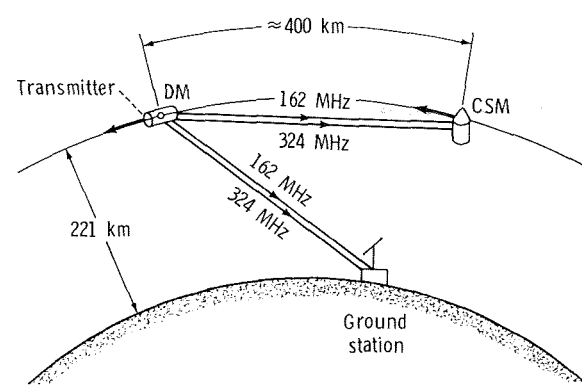

FIGURE 10-14.—Schematic diagram of Doppler links.

2. To measure the time changes of the spacecraft-to-ground columnar electron content, from which an averaged columnar content and the electron density at the DM could be derived under some simplifying assumptions. (Because horizontal gradients at orbital heights were measured simultaneously, a secondary goal was to investigate the increase in accuracy obtained by performing these inversions.)

3. To observe traveling ionospheric disturbances with both the DM-to-CSM and the DM-to-Earth links.

4. To detect boundaries of turbulent regions of the ionosphere, such as the aurora oval and the equatorial region.

The data-collection phase of the experiment was highly successful. The DM-to-CSM link collected samples of differential Doppler data over a period of nearly 14 hours from nine orbital revolutions on July 24. Through the courtesy of the Defense Mapping Agency, DM dual-frequency emissions were recorded on Earth by eight Tranet and geoceiver tracking stations on 235 passes. Table 10-III contains orbital data for both the DM and the CSM.

Consistent with preflight expectations, the resolution of the Doppler measurements was $1\sigma \approx 3$ mHz in 10-second integration time. The oscillators of the Doppler links performed as specified, with a stability of a few parts in 10^{12} over a 10- to 100-second integration interval.

Block diagrams of the instrumentation can be found in reference 10-23. Figure 10-15 is a schematic representation of the raw data used in the experiment, and the data-reduction and data-processing flow adopted is shown in figure 10-16.

The differential Doppler shift is defined as $\delta\dot{\Phi} = \dot{\Phi}_1 - (f_1/f_2)\dot{\Phi}_2$ where $\dot{\Phi}_1$ and $\dot{\Phi}_2$ are the Doppler shifts at the higher (f_1) and lower (f_2) frequencies of the link. In this case, $f_1 = 324$ MHz and $f_2 = 162$ MHz; therefore,

$$\delta\dot{\Phi} = \dot{\Phi}_1 - 2\dot{\Phi}_2 \qquad (10\text{-}24)$$

In the path from the DM to the CSM, the following relationship applies:

$$\delta\dot{\Phi} = \left(40.3/2\lambda_1\right)\left[\left(1/f_2^{\,2}\right) - \left(1/f_1^{\,2}\right)\right] d/dt \int_{DM}^{CSM} N\, ds \qquad (10\text{-}25)$$

where wavelength $\lambda_1 = c/f_1$, c being the velocity of light in free space.

Under the assumptions that the two terminals of the link were in nearly coincident circular orbits and that the temporal variations of the ionosphere could be disregarded while the Doppler samples were being taken, the differential Doppler shift $\delta\dot{\Phi}$ is a measure of the electron-density gradients at the ASTP orbital altitude averaged over a length Δx corresponding to the integration time of the Doppler sample:

$$\frac{\overline{\partial N}}{\partial x} = \frac{\lambda_1 f_1^{\,2} f_2^{\,2}}{40.3\left(f_2^{\,2} - f_1^{\,2}\right)} \frac{\delta\dot{\Phi}}{v_0\, \Delta x} \qquad (10\text{-}26)$$

where v_0 is the common orbital velocity of the two terminals. The applicable equations for DM-to-Earth paths are provided in reference 10-25.

Figures 10-17 and 10-18 represent the DM-to-CSM differential Doppler records obtained during revolutions 127 and 131. Table 10-IV contains the starting time of each orbit and the serial number of the frame and word recorded when the DM crossed the meridian containing the subsolar point (SSP). Each frame has 73 words, each 10 seconds long, so that, for example, the start of revolution 126 corresponds to $(47 \times 73 + 31) \times 10 = 34\ 620$ seconds from reference time zero, which was set at the beginning of the link operation.

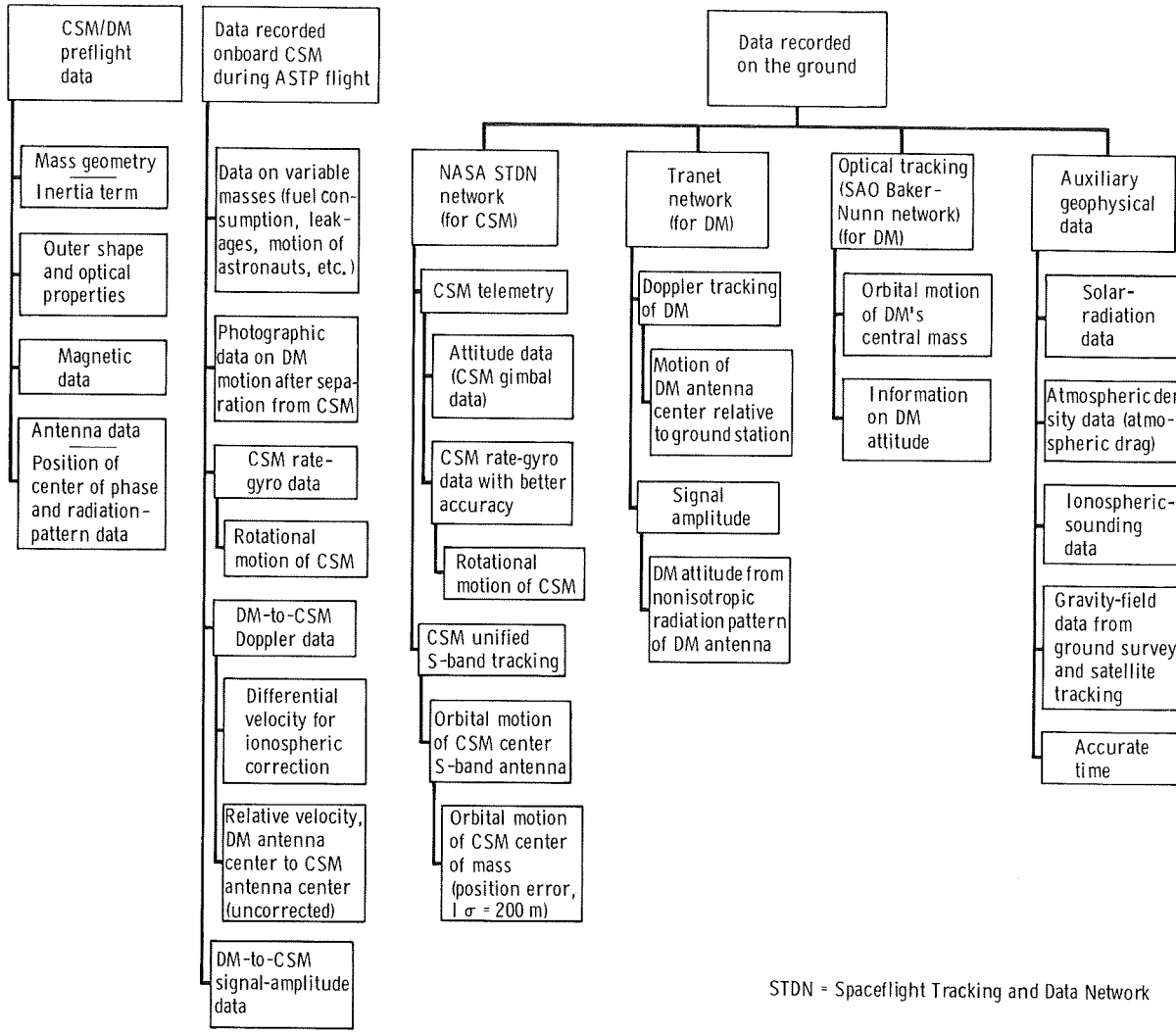
CSM/DM preflight data
Mass geometry
Inertia term
Outer shape and optical properties
Magnetic data
Antenna data
Position of center of phase and radiation-pattern data
Data recorded onboard CSM during ASTP flight
Data on variable masses (fuel consumption, leakages, motion of astronauts, etc.)
Photographic data on DM motion after separation from CSM
CSM rate-gyro data
Rotational motion of CSM
DM-to-CSM Doppler data
Differential velocity for ionospheric correction
Relative velocity, DM antenna center to CSM antenna center (uncorrected)
DM-to-CSM signal-amplitude data
Data recorded on the ground
NASA STDN network (for CSM)
CSM telemetry
Attitude data (CSM gimbal data)
CSM rate-gyro data with better accuracy
Rotational motion of CSM
CSM unified S-band tracking
Orbital motion of CSM center S-band antenna
Orbital motion of CSM center of mass (position error, 1 σ = 200 m)
Tranet network (for DM)
Doppler tracking of DM
Motion of DM antenna center relative to ground station
Signal amplitude
DM attitude from nonisotropic radiation pattern of DM antenna
Optical tracking (SAO Baker-Nunn network) (for DM)
Orbital motion of DM's central mass
Information on DM attitude
Auxiliary geophysical data
Solar-radiation data
Atmospheric density data (atmospheric drag)
Ionospheric-sounding data
Gravity-field data from ground survey and satellite tracking
Accurate time
STDN = Spaceflight Tracking and Data Network

FIGURE 10-15.—Block diagram of the raw data.

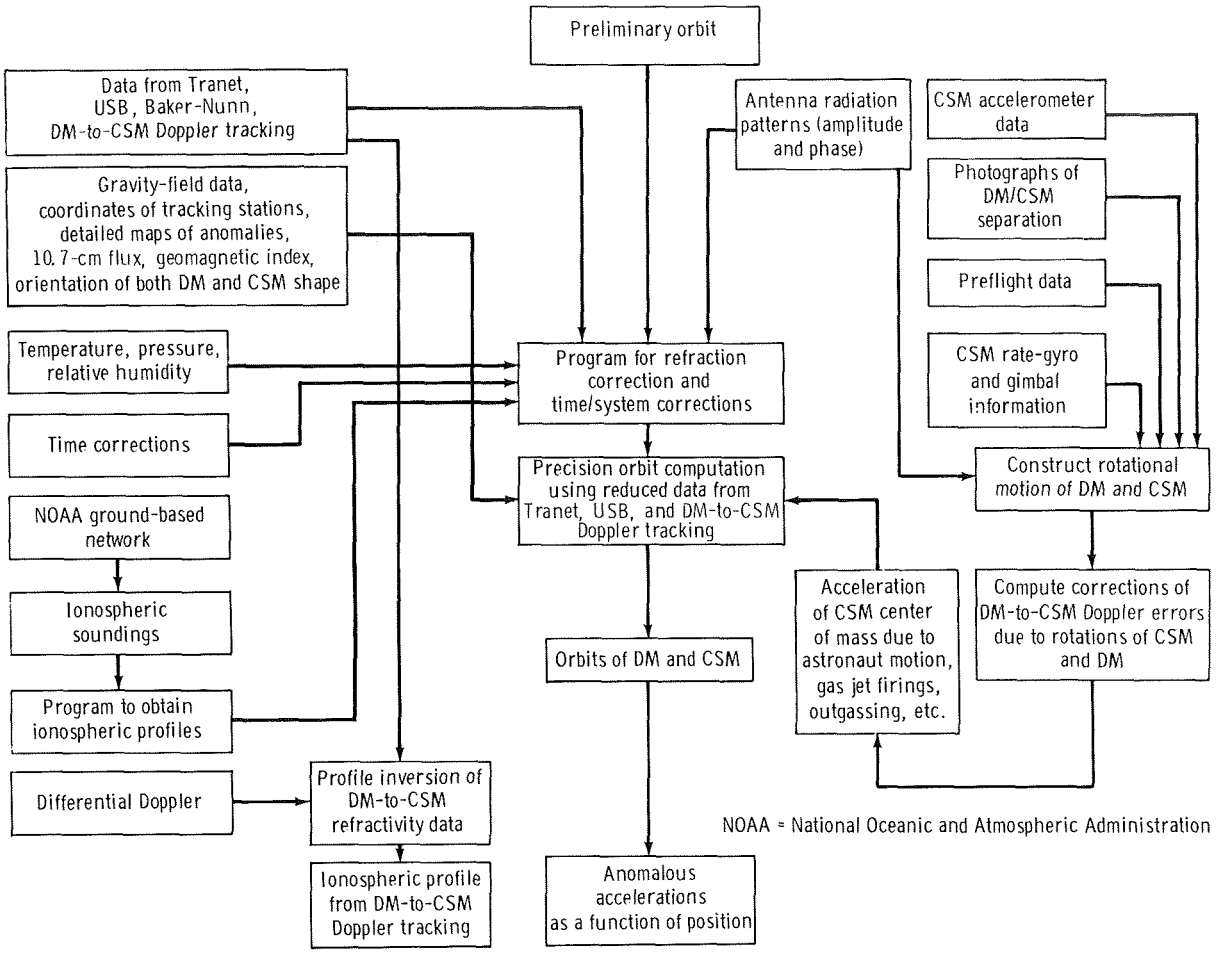
Preliminary orbit
Data from Tranet, USB, Baker-Nunn, DM-to-CSM Doppler tracking
Antenna radiation patterns (amplitude and phase)
CSM accelerometer data
Gravity-field data, coordinates of tracking stations, detailed maps of anomalies, 10.7-cm flux, geomagnetic index, orientation of both DM and CSM shape
Photographs of DM/CSM separation
Preflight data
Temperature, pressure, relative humidity
Program for refraction correction and time/system corrections
CSM rate-gyro and gimbal information
Time corrections
Precision orbit computation using reduced data from Tranet, USB, and DM-to-CSM Doppler tracking
Construct rotational motion of DM and CSM
NOAA ground-based network
Ionospheric soundings
Acceleration of CSM center of mass due to astronaut motion, gas jet firings, outgassing, etc.
Compute corrections of DM-to-CSM Doppler errors due to rotations of CSM and DM
Orbits of DM and CSM
Program to obtain ionospheric profiles
Differential Doppler
Profile inversion of DM-to-CSM refractivity data
NOAA = National Oceanic and Atmospheric Administration
Ionospheric profile from DM-to-CSM Doppler tracking
Anomalous accelerations as a function of position

FIGURE 10-16.—Simplified diagram of data reduction and processing.

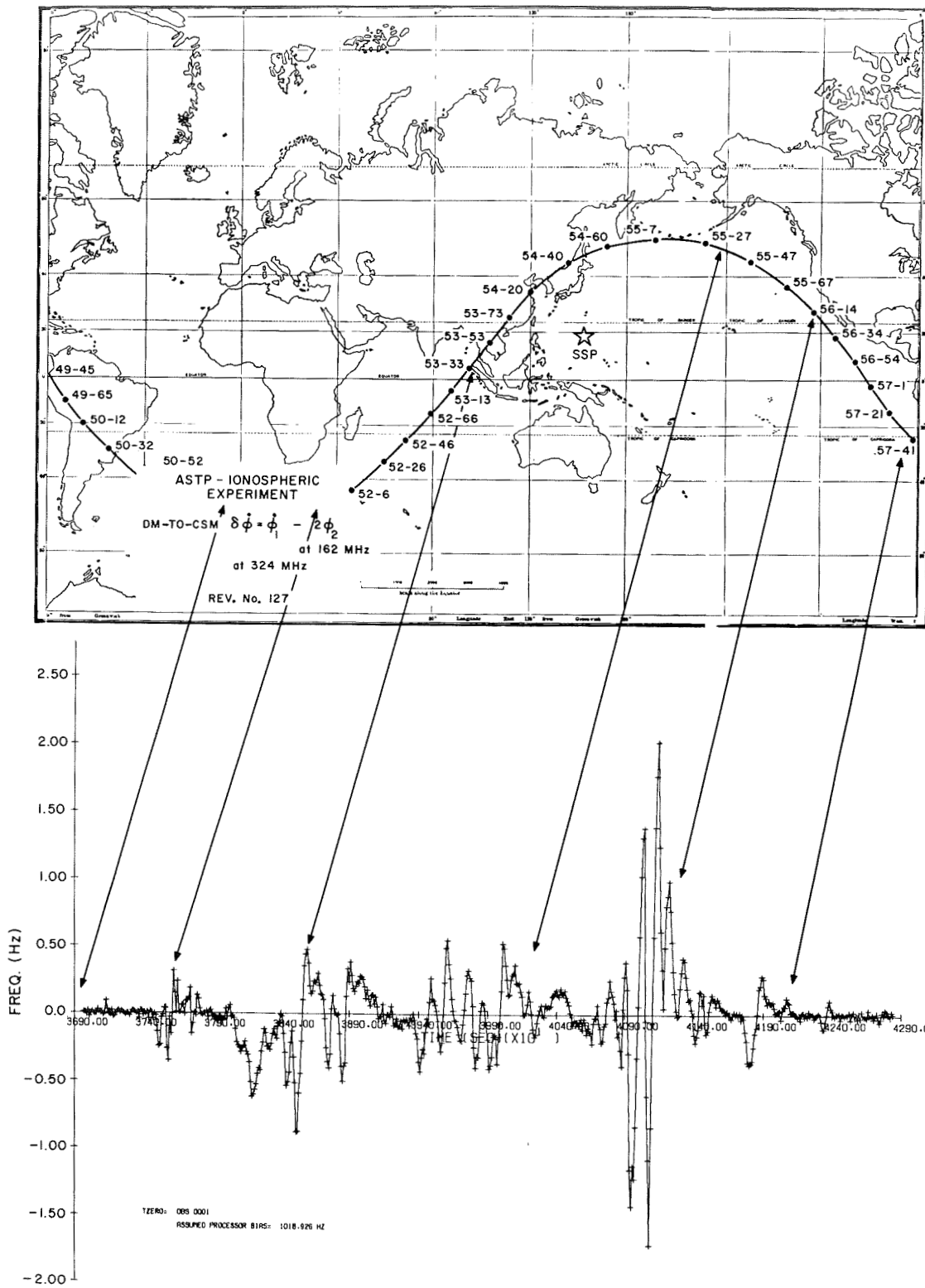

FIGURE 10-17.—Map of revolution 127 with differential Doppler plot.

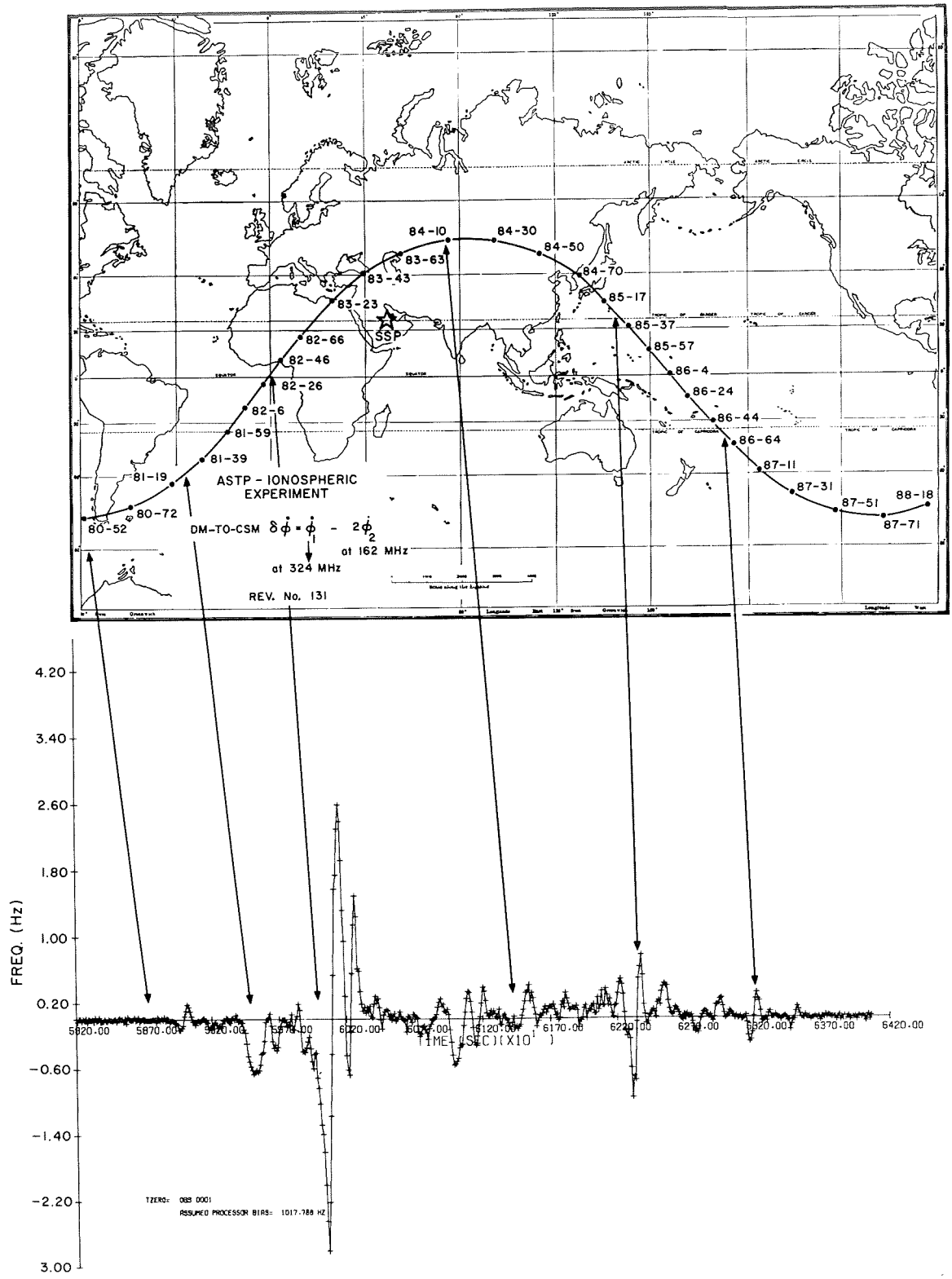

FIGURE 10-18.—Map of revolution 131 with differential Doppler plot.

It can be seen that sharp horizontal gradients of electron density have been detected. From equation (10-26), $\overline{\partial N}/\partial x = 2.62 \times 10^5 \times \delta\Phi$ electrons/m^3/m. The figures show that gradients as large as $\approx 10^6$ electrons/m^3/m are not uncommon for a day such as July 24, which was magnetically quiet and was characterized by an electron density at a 220-km height that varied from $\approx 3 \times 10^9$ electrons/m^3 (nightside) to $\approx 5 \times 10^{11}$ electrons/m^3 (dayside). Most of the gradients are encountered at the equatorial crossings and are most likely related to the equatorial F-layer irregularities.

The nine-cycle waveform shown in figure 10-17 is suggestive of a dayside traveling ionospheric disturbance characterized by the following parameters (preliminary model).

Parameter	*Value*
Apparent spatial wavelength along the orbital track at 220-km height, km	≈ 800
Estimate of the spatial wavelength as it would be observed from the ground, km	690
Spatial extent along the orbital track at 220-km height, km	≈ 7200
Estimate of peak-to-peak electron-density perturbation, percent	35
Estimate of velocity, m/sec	≈ 700
Estimate of the period as it would be observed from the ground, min	16

During the ASTP ionospheric experiment, the first spacecraft-to-spacecraft horizontal sounding of the ionosphere at a height of 220 km was performed. In addition, data were acquired that are expected to add new and useful information to the literature on ionospheric electron-density structures at a height that is important and that had never been probed before. Furthermore, it is expected that the experiment will contribute to a better understanding of the manner in which horizontal gradients of electron density influence the accuracy of ionospheric columnar measurements performed by transmitting radio emissions from satellites to the Earth.

At the time this report was written, analysis was continuing both for the data collected with the DM-to-CSM link and for the space-to-ground data collected by the ground-based network of stations that participated in the experiment.

Results From the Gravimetric Experiment

Among the effects controlling the satellite-to-satellite relative velocity are local variations in gravity. Experiment MA-089 was designed to detect anomalous gravity, i.e., gravity-field variations having wavelengths between 250 and 1000 km. The observed Doppler shift, or velocity difference, also contains other large variations due to the gross relative orbital motion and to the relative motion of the transmitting and receiving antennas with respect to the centers of mass of the CSM and the DM. Additional contributors to the observed relative velocity are the radiation patterns of the antennas and other accelerations on the vehicles (such as air drag, radiation pressure, and astronaut motion). As the analysis proceeded, each of these effects was eliminated, leaving a clean Doppler signal that was free of all extraneous effects and contained the Doppler shift due to anomalous gravity.

Estimated gravity signal.—In the section entitled "The Gravity Field From Satellite-to-Satellite Velocity Measurements," general considerations were used to estimate the gravity signal expected to be detected by means of Experiment MA-089. More detailed simulations were performed during the data-analysis phase of the experiment. These simulations included the actual satellite configuration and physical characteristics, such as the area-to-mass ratio, and environmental factors, such as the atmospheric density. From these simulations, for example, for a satellite spacing of 310 km, a satellite height of 210 km, and a gravity anomaly of 1 mm/sec^2 (100 mgal) in a 100-by 100-km block, a peak-to-peak variation of 1.00 mm/sec should be observable when the satellite pair is directly over an anomaly. Such anomalies

are common; 69 anomalies greater than 1.5 mm/sec^2 (150 mgal) have been observed in terrestrial data, and fourteen 100- by 100-km anomalies greater than 2 mm/sec^2 (200 mgal) have been found. For a 300- by 300-km, 1-mm/sec^2 (100 mgal) anomaly, the peak-to-peak variation would be 7.05 mm/sec; no anomalies of this size and magnitude have been observed. Although detailed calculation of the peak-to-peak variation in velocity requires use of numerical-integration programs, it can be approximated by

$$\Delta v \propto \frac{L^2}{2} \overline{\Delta g_0} \frac{x\ \Delta x}{r^3} \qquad (10\text{-}27)$$

Here, L is the half-width of the mean gravity anomaly $\overline{\Delta g_0}$, x is the downtrack distance, r is the distance of the midpoint of the two satellites from the anomaly, and Δx is the distance between the spacecraft. Therefore, the signal is roughly proportional to the gravity anomaly and the spacecraft spacing and is proportional to the square of the anomaly size.

The preceding estimate is a measure of the effect of a single gravity anomaly. Because Experiment MA-089 was sensitive to many anomalies, a granularity was produced in the observed Doppler signal. The root mean square of this granularity was calculated for a number of orbital tracks from a fine-grained gravity model based on the observed 1° by 1° anomalies. The additional short-wavelength signal has an rms of 2.1 mm/sec.

Error budget.—When the 11 000-second duration of data take (while the CSM and the DM were still connected) was adopted as the integration time, an rms noise level of 2.26 mm/sec was found. When an integration time of 10 to 100 seconds was used, a noise level of 1.8 mm/sec was obtained. These results are consistent with the expected behavior of the oscillator at the two integration times considered. These data are shown in figure 10-19. The Fourier transform of the 11 000-second-long sample has little structure, with a mild maximum near 300 seconds. Since the signal strength during this data-take interval was very large, the previously indicated noise levels can be attributed to oscillator stability.

A worst-case signal-to-noise ratio for the data with the CSM antenna misalined by 35° with respect to the DM and with no multipath is as follows:

Separation	*162 MHz*	*324 MHz*
350 km	37 dB	31 dB
500 km	33 dB	27 dB

System design required, as a minimum, a 22-dB signal-to-noise ratio. For a worst-case 500-km separation, the contribution is 2.32 mm/sec.

The multipath effects are variegated; first of all, they influence the signal-to-noise ratio as follows:

Separation	*162 MHz*	*324 MHz*
350 km	29 dB	23 dB
500 km	23 dB	17 dB

In addition, there is a multipath-induced error due to the erratic behavior of a phase-lock loop if several carriers are present within its bandwidth. Multipath, if present, would boost the total error to 3.50 mm/sec. However, multipath can occur only over the ocean, which is a good reflecting surface for very high frequencies. No discernible difference appeared between the noise level over land and that over oceans, so multipath was ruled out.

Therefore, an expected signal of 2.1 mm/sec, for a 1-mm/sec^2 (100 mgal) anomaly, and an expected noise of 2.32 mm/sec produce a signal-plus-noise to noise ratio of only 1.26 in a 100-second integration time. Consequently, Experiment MA-089 can be expected to reveal reliably only gravity signatures larger than 1 mm/sec^2 (100 mgal), and those are, unfortunately, not expected to be numerous.

Data analysis.—The Doppler signal observed after ionospheric effects had been removed is given in figure 10-10. The data spanned 48 910 seconds with 4891 data points, and 83 individual points were eliminated. The equipment lost lock twice. The relative velocity of the two spacecraft is quite evident in the figure, thus demonstrating to zeroth order that the experiment obtained good data.

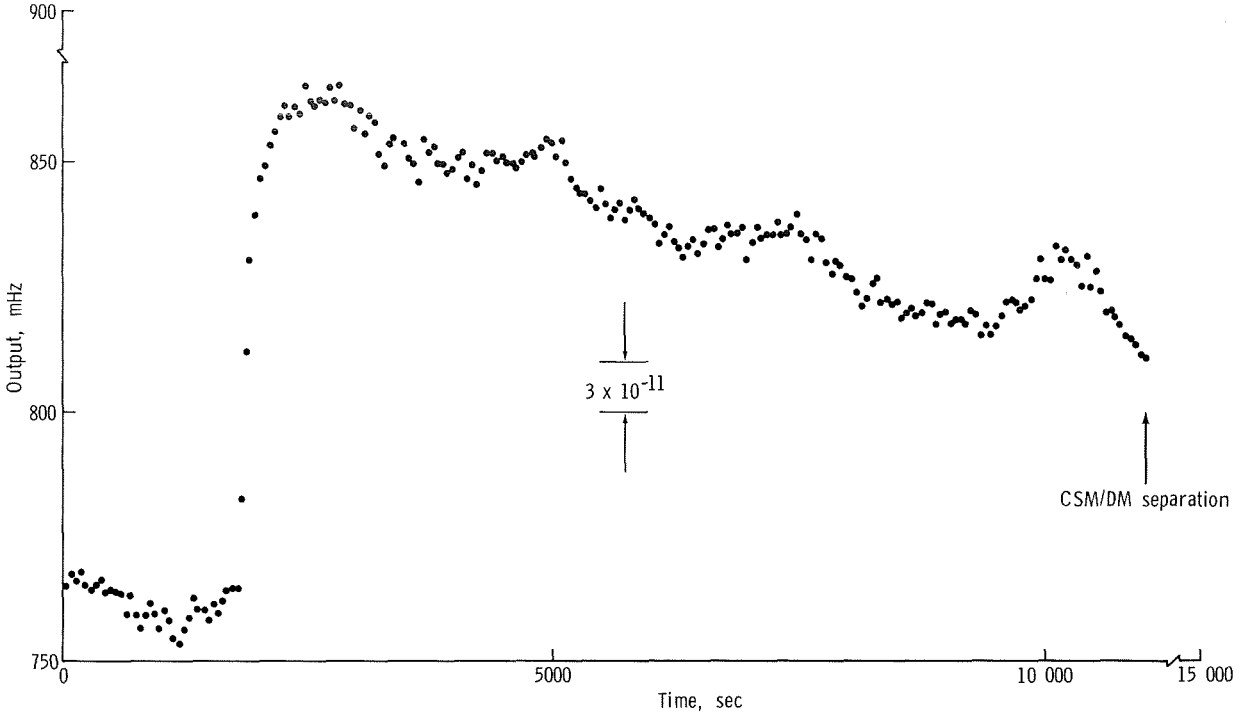

FIGURE 10-19.—Initial 11 000 seconds of 324-MHz Doppler data. Vertical scale shows the output of the receiver Doppler processor with a 1020-Hz instrument bias subtracted.

As described in the section entitled "Data Reduction," the data were processed in a series of steps. In the first level, the gross orbital data were subtracted and an rms Doppler signal of 1.5 m/sec was left, consistent with the accuracy of the orbits derived from ground tracking data. These residuals are given in figure 10-20(a). The long-period orbital effects were further reduced by means of polynomial smoothing, in which the orbital velocity determined from ground tracking data was used as the argument. This smoothing effectively eliminated all observable orbital effects, leaving an rms signal of 49 mm/sec, as shown in figure 10-20(b).

The second level of processing removed the Doppler shift due to the rotation of the DM antenna about the center of mass and to the antenna pattern. A high-pass filter, designed to pass all frequencies in the Fourier transform with periods shorter than 400 seconds, was applied to all the data. This filtering corresponds, roughly, to eliminating gravity signatures 3000 km and longer. When the DM dynamics analysis was repeated by using unfiltered data, the same results were found. The Fourier transform of these filtered data is given in figure 10-21, in which the spectral lines associated with the DM rotation are easily identified. The width of the lines is, in part, attributable to the facts that the rotational period of the DM continually increased during data acquisition and that the period changed discontinuously as the satellite passed from sunlight to Earth shadow.

Because of these two rotational-period effects, the velocity data were analyzed in sections. The orbit was divided into 17 intervals, 9 of complete Sun illumination and 8 of complete shadow. By using the periods and their rate of change determined by a Fourier transform of the data, the periodic velocity variations were computed and subtracted from the data. The periods of rotation for each Sun/shadow interval are shown in table 10-V. Amplitudes of the components are given in table 10-VI. The phase of each component is not given, since it refers to an arbitrary origin. The internal consistency of the amplitudes and the

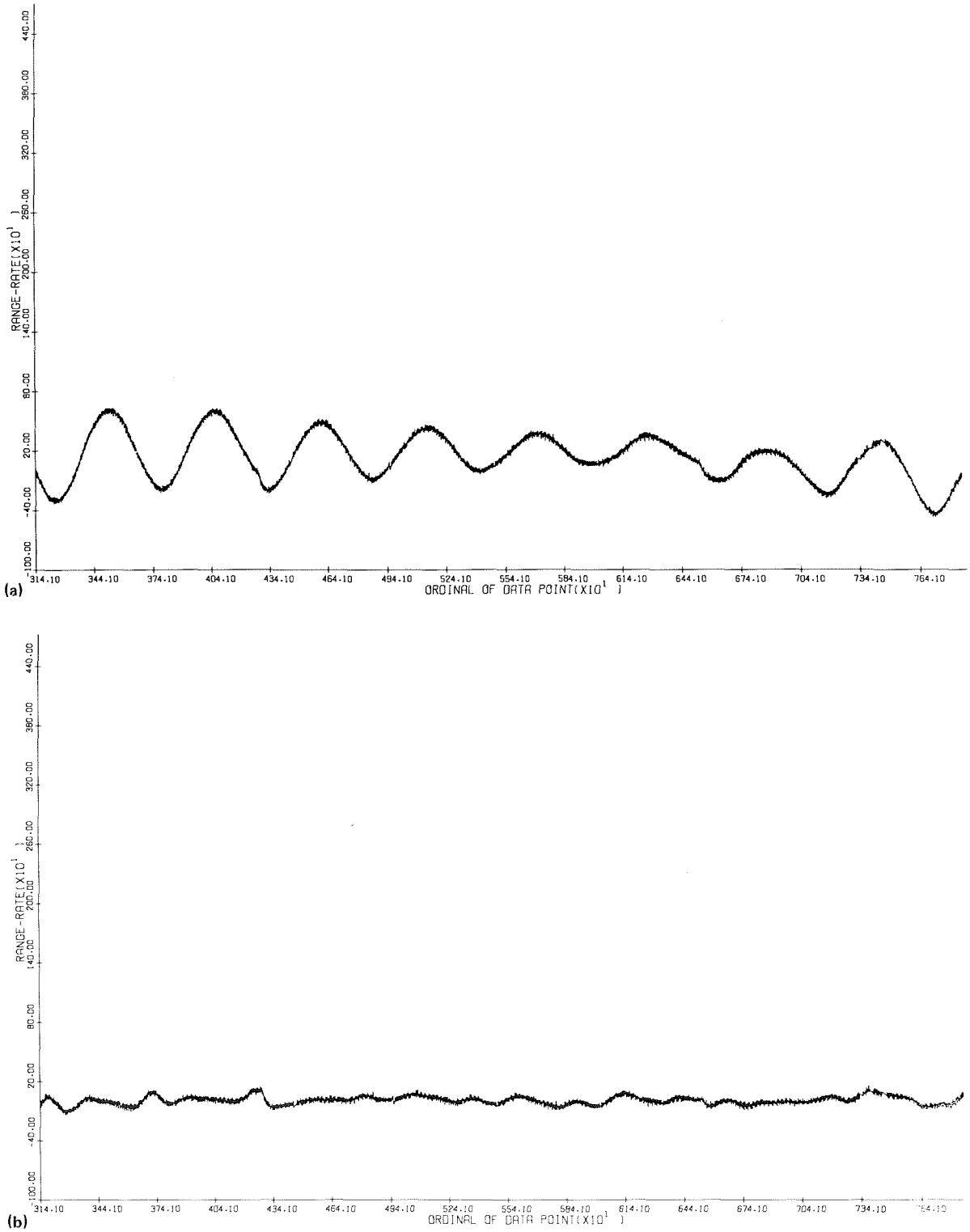

FIGURE 10-20.—Relative velocity after removal of ionospheric and orbital effects. (a) Before polynomial smoothing. (b) After polynomial smoothing.

periods strongly suggests that the investigators' understanding of the dynamics of the DM rotation and the antenna radiation pattern was correct. Figure 10-13 is a typical Fourier transform of one section of the reduced data. Table 10-VII also includes the rms signals for each subset of data; the values range from 9.41 to 11.80 mm/sec.

During data acquisition, the CSM was three-axis stabilized, rolling 360° per orbital revolution to keep the receiver antenna pointed toward the DM. A sample of rate-gyro data is shown in figure 10-22. Pitch and yaw were typically similar, seldom exceeding 0.05°/sec. Roll remained close to 0.06°/sec, the orbital rate.

Because the center of the receiving antenna was 475 mm from the center of gravity, measured along the longitudinal axis, a pitch rotation of 0.05°/sec would result in an antenna line-of-sight motion of only 0.4 mm/sec. Simultaneous pitch and yaw could raise this value to approximately 0.6 mm/sec because the antenna was approximately halfway between the y-axis and the z-axis. Because of the small amplitude of these motions, they were not modeled.

The primary contribution from atmospheric density to the Doppler signal was at the orbital period. This information was completely removed during orbit computation, polynomial smoothing, and high-pass filtering. To contribute to the observed noise spectrum, any remaining local variations in atmospheric density would have to be of the order of the density with 100-km wavelength. Gravity waves or microstructures of this magnitude and wavelength are extremely unlikely at these altitudes.

From the Fourier spectra shown in figures 10-13 and 10-21, it can be seen that significant energy remains in the frequency band around 1/24 sec^{-1}. This energy could be residual noise from the 24-second signal generated by the third harmonic of the DM antenna radiation pattern or aliasing of periods shorter than $1/f_n$, the reciprocal Nyquist frequency. A high-frequency signal at this level is not anticipated to be due to the Earth's gravity field. In any event, this spectral energy was eliminated.

To remove the high-frequency noise, a filter, centered on 24 seconds, was constructed to subtract periods less than 30 seconds. This filter was applied n times to give an rms approaching $(2.1^2 + 2.82^2)^{1/2} = 3.6$ mm/sec, corresponding to expectations. The resulting changes in the rms scatter are shown in table 10-VII.

A typical time history of the filtered data is given in figure 10-12, in which no obvious structure that could be interpreted as a gravity signal can be seen. As a further test of the validity of the observations, a predicted Doppler shift was generated from surface-gravity observations, and a

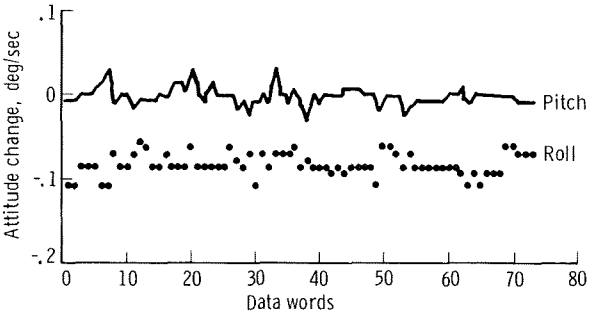

FIGURE 10-22.—Pitch and roll data for CSM from frame 60.

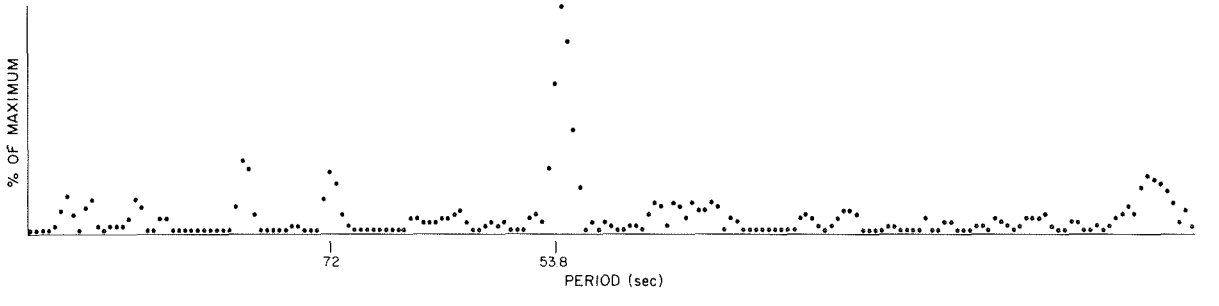

FIGURE 10-21.—Fourier spectrum of smoothed data showing effects of DM rotation.

TABLE 10-V.—DM Rotational Periods

Time, MJD	*Interval*	*Periods, sec*					*State*
		53	*24*	*72*	*36*	*108*	
42617.0699	1	53.094	23.656	71.457	35.908	108.609	Sunlight
42617.1060	2	53.222	23.755	71.345	34.930	109.155	Shadow
42617.1315	3	53.331	23.811	71.779	36.080	109.189	Sunlight
42617.1677	4	53.483	23.868	71.426	35.894	109.494	Shadow
42617.1931	5	53.547	23.940	72.016	36.246	109.661	Sunlight
42617.2293	6	53.695	23.993	71.763	36.019	109.952	Shadow
42617.2548	7	53.790	24.046	72.351	36.400	109.525	Sunlight
42617.2909	8	53.865	24.087	71.880	35.745	110.411	Shadow
42617.3164	9	53.953	24.168	72.562	36.542	109.828	Sunlight
42617.3525	10	54.049	24.188	72.202	36.065	110.709	Shadow
42617.3780	11	54.132	24.233	72.954	36.691	110.595	Sunlight
42617.4142	12	54.234	24.261	72.625	36.212	111.719	Shadow
42617.4396	13	54.343	24.388	73.303	36.795	111.107	Sunlight
42617.4758	14	54.359	24.398	72.812	36.816	111.770	Shadow
42617.5012	15	54.657	24.470	73.619	36.984	111.180	Sunlight
42617.5374	16	54.596	24.405	73.058	36.635	110.381	Shadow
42617.5629	17	54.844	24.560	73.820	37.133	111.766	Sunlight

TABLE 10-VI.—Amplitudes of DM Rotational Components for Five Periods

Time, MJD	*Interval*	*Amplitude, mm/sec, for period of—*				
		108 sec	*72 sec*	*53 sec*	*36 sec*	*24 sec*
42617.0699	1	6.33	4.82	19.62	5.74	6.73
42617.1060	2	5.76	5.13	19.98	6.68	6.05
42617.1315	3	5.58	5.00	19.91	5.58	7.33
42617.1677	4	5.50	4.19	20.59	5.39	6.58
42617.1931	5	5.90	5.54	18.80	5.60	7.55
42617.2293	6	5.62	5.14	20.16	6.14	6.58
42617.2548	7	6.14	5.08	18.88	5.36	7.70
42617.2909	8	5.38	4.72	19.73	6.47	6.81
42617.3164	9	5.29	5.45	19.73	5.90	8.00
42617.3525	10	5.24	5.38	20.63	7.24	7.85
42617.3780	11	5.24	5.15	19.59	5.78	8.30
42617.4142	12	5.00	5.20	20.96	7.39	8.75
42617.4396	13	5.82	5.50	20.00	6.32	6.66
42617.4758	14	5.20	6.26	17.93	7.41	8.23
42617.5012	15	4.55	6.09	18.73	5.69	6.73
42617.5374	16	3.98	3.15	15.84	5.13	7.10
42617.5629	17	5.20	6.07	17.50	8.80	8.45

TABLE 10-VII.—Root Mean Square of $\dot{\rho}$ Residuals After Multiple Filtering

[*Values in millimeters per second*]

Interval	*Number of filter applications*				
	0	*1*	*4*	*6*	*8*
1	9.41	6.03	5.26	5.11	5.01
2	10.27	6.61	6.11	6.03	5.98
3	9.56	6.05	5.15	4.98	4.86
4	11.80	9.41	9.03	8.96	8.91
5	10.09	7.17	6.38	6.16	6.01
6	10.20	6.30	5.40	5.22	5.12
7	11.27	8.38	7.65	7.46	7.34
8	10.20	5.96	5.04	4.83	4.69
9	10.03	6.29	5.41	5.21	5.08
10	9.80	5.38	4.52	4.35	4.24
11	10.15	6.49	5.57	5.37	5.24
12	9.97	5.67	4.77	4.56	4.42
13	9.99	6.99	6.07	5.86	5.72
14	9.84	5.42	4.53	4.40	4.33
15	10.13	7.54	6.43	6.08	5.85
16	9.94	8.76	7.45	7.09	6.84
17	9.73	5.90	4.92	4.74	4.64

cross-correlation function, based on a single anomaly, was calculated. The result is a cross correlation not significantly different from zero; in other words, the predicted velocity would correlate equally well with many subsets of the data.

A summary of the data analysis appears in table 10-VIII, which gives the rms left after each step of the reduction. The noise remaining in the data is too large for any firm conclusion to be drawn about the Earth's gravity field.

CONCLUSIONS

The Doppler Tracking Experiment had two goals: (1) to perform a feasibility test of the low-low satellite-to-satellite method as a scheme capable of measuring gravity-field anomalies and (2) to perform satellite-to-satellite horizontal sounding of the ionosphere.

The ionospheric data collected during the experiment are of excellent quality. The differential Doppler noise was as low as expected, and the experiment provided valuable satellite-to-satellite observations, never made before, of wave phenomena occurring in the ionosphere at the ASTP orbital height.

The gravity data were, on the contrary, corrupted by a level of single-frequency Doppler noise higher than expected. No good explanation for this occurrence has yet been found, but whatever its origin, this high level of noise has thus far prevented any reliable identification of gravity-anomaly signatures in the data.

TABLE 10-VIII.—Root Mean Square of the Data After Each Analysis Step

Step	*Effect removed*	*rms, mm/sec*
1	Gross orbital motion	48
2	Low-frequency noise	18
3	DM rotation	[a]7 to 12
4	High-frequency noise	3.6
	Anticipated value	3.6

[a] After step 3, the noise level was too high for any signal to be observed. Presumably, step 4, consisting of four applications of a low-pass filter, in addition to eliminating the high-frequency noise, also removed an excessive amount of the desired signal.

Ionospheric Experiment

The results of the ionospheric experiment are as follows:

1. Changes in the columnar electron content between the two spacecraft were accurately measured. From these, horizontal gradients of electron density at the height of 220 km were derived. Gradients as high as 10^6 electrons/m^3/m were repeatedly observed both in the dayside ionosphere (typical density of approximately 5×10^{11} electrons/m^3) and in the nightside ionosphere (typical density of approximately 3×10^9 electrons/m^3). Most of these gradients were encountered at the equatorial crossings and are most likely related to equatorial F-layer irregularities.

2. Traveling ionospheric disturbances were

detected. Most noticeable was a nine-cycle ionospheric wave found off the coast of California during revolution 127 (frame 56, word 14, July 24, 1975, 01:54:36 UT), characterized by a peak-to-peak electron-density perturbation of 35 percent, by a wavelength of 690 km (as the traveling ionospheric disturbance would be observed from the ground), and by a spatial extent of approximately 7200 km along the ASTP orbital track.

3. Spacecraft-to-ground differential Doppler data were collected for SAO by the Defense Mapping Agency from 235 passes of the docking module, covering the entire surface of the Earth. Although the processing of the data has not yet been completed, the investigators are confident that this part of the ASTP ionospheric experiment will contribute to the understanding of the manner in which horizontal gradients of electron density influence the accuracy of the ionospheric columnar measurements performed by using radio emissions from satellites to the Earth. The results of this part of the experiment will be published in the technical literature.

Gravity Experiment

The gravity-experiment results are summarized as follows:

1. Detailed computations verified that a 1-mm/sec^2 (100 mgal), 1° by 1° gravity anomaly would give rise to a 1.00-mm/sec peak-to-peak differential velocity for the two spacecraft.

2. The satellite-to-satellite range-rate measurement was made. The equipment revealed gross orbital motion, which was verified at a 1-m/sec level with orbits determined independently from unified S-band and Doppler data. After the gross long-period effects had been eliminated with these independent orbits, the satellite-to-satellite data had an rms (signal plus noise) of 48 mm/sec.

3. The differential Doppler signal due to the motion of the CSM about its center of mass was always within 1 mm/sec, as specified.

4. The tumbling motion of the DM about its center of mass was very clearly discernible in the Doppler observations. The Fourier transform of the data is given in figure 10-21. The principal periods were as follows:

Approximate period	*Phenomenon*
72 seconds	Spin rate around the CSM
208 seconds	Period of precession
53 seconds	Harmonics combination of 72- and 208-second periods
36 seconds	Second harmonic of the 72-second period due to tesseral harmonics of the antenna radiation pattern
24 seconds	Third harmonic of the 72-second period due to tesseral harmonics of the antenna radiation pattern

Detailed analysis of the Fourier spectra revealed a significant lengthening of the period over the lifetime of the mission and a significant change in the rotational period of the DM as it passed from shadow to sunlight and vice versa. Figure 10-23 contains the mean period for each complete sunlight and shadow portion. The consequence of this large variation is that the phase of the motion and, to a lesser extent, the amplitude are not preserved throughout the mission; therefore, analysis of each orbital segment must be performed separately.

5. Once the periodic motions were removed, the total system noise was found to be between 9.41 and 11.80 mm/sec for each subset taken separately.

6. The Doppler residuals for a sample of the data set are given in figure 10-12. The remaining noise level, both from a scan of the figure and from the Fourier statistics, precludes an unambiguous detection of specific gravity anomalies. This fact applies to both filtered and smoothed data.

7. One explanation for the high noise level is the degradation of one or both of the satellite

oscillators. As discussed in the section entitled "Orbit Determination," frequency offsets were recovered from the ground tracking data. Although a relatively high rejection rate of passes did occur, the stability of the transmit oscillator was measured to be within specification.

8. The main conclusion is that the total system noise level was sufficiently large to prevent detection of gravity anomalies. Attempts to determine the source of the noise level were not successful. The Fourier spectra of the residuals revealed no significant energy density, showing only clustered broadband noise. The DM motion about its center of gravity has been completely understood, to the point of determining its physical parameters (moments of inertia, antenna position, spin rate, and antenna radiation patterns). Therefore, a plausible explanation for this high noise level remains unidentified as yet. It can be concluded that, with the spatial wavelength implied by the CSM/DM separation, gravity anomalies at the ASTP orbital height produce intervehicular range rates of less than 2.32 mm/sec. This undesirably high threshold sensitivity is, in part, determined by the fact that the stability of the oscillator worsens as the integration time increases beyond 100 seconds.

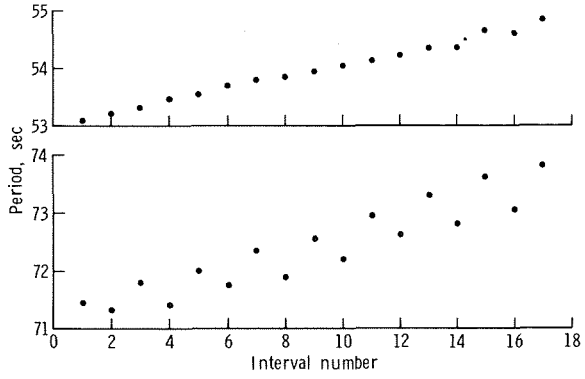

FIGURE 10-23.—Mean period for each sunlight and shadow portion of the DM rotation for 53- and 72-second periods. (See table 10-V.)

REFERENCES

10-1. Isacks, Bryan; Oliver, Jack; and Sykes, Lynn R.: Seismology and the New Global Tectonics. J. Geophys. Res., vol. 73, no. 18, Sept. 15, 1968, pp. 5855-5899.

10-2. Muller, P. M.; and Sjogren, W. L.: Mascons: Lunar Mass Concentrations. Science, vol. 161, no. 3843, Aug. 16, 1968, pp. 680-684.

10-3. Schwarz, C. R.: Gravity Field Refinement by Satellite to Satellite Doppler Tracking. NASA CR-117404, 1970.

10-4. Wolff, Milo: Direct Measurements of the Earth's Gravitational Potential Using a Satellite Pair. J. Geophys. Res., vol. 74, no. 22, Oct. 15, 1969, pp. 5295-5300.

10-5. Comfort, G. C.: Direct Mapping of Gravity Anomalies by Using Doppler Tracking Between a Satellite Pair. J. Geophys. Res., vol. 78, Oct. 10, 1973, pp. 6845-6851.

10-6. Vonbun, F. O.: The ATS-F/Nimbus-E Tracking Experiment. Rotation of the Earth, Paul Melchior and Shigeru Yumi, eds., D. Reidel Publ. Co. (Dordrecht, Holland), 1972, pp. 112-120.

10-7. Jackson, John E.; and Seddon, J. Carl: Ionosphere Electron Density Measurements With the Navy Aerobee Hi Rocket. J. Geophys. Res., vol. 63, no. 1, Mar. 1958, pp. 197-208.

10-8. Seddon, J. C.: Propagation Measurements in the Ionosphere With the Aid of Rockets. J. Geophys. Res., vol. 58, 1953, pp. 323-335.

10-9. Alpert, Ya. L.: A Method for Investigating the Ionosphere With Artificial Satellites. Usp. Fiz. Nauk, vol. 64, 1958, p. 3.

10-10. Alpert, Ya. L.: On the Results of Ionosphere Investigations With the Help of Coherent Radio Waves Emitted by Satellites. Space Research V, Proceedings of the Fifth International Space Science Symposium, D. S. King-Hele, P. Muller, and G. Righini, eds., North-Holland Publishing Co. (Amsterdam), 1965, pp. 652-686.

10-11. Alpert, Ya. L.: Radio Wave Propagation in the Ionosphere. The Ionosphere. vol. 1. second ed. Consultants Bureau (New York), 1973, pp. 61-77.

10-12. Alpert, Ya. L.: On Radio Methods of Ionospheric Investigations by Means of Coherent Radio Waves Emitted by Satellites. Paper presented at COSPAR/URSI Symposium on Beacon Satellite Investigations of the Ionosphere Structure and ATS-6 Data (Moscow), Nov. 1974.

10-13. Garriott, Owen K.: The Determination of Ionospheric Electron Content and Distribution From Satellite Observations, Part 1, Theory of the Analysis. J. Geophys. Res., vol. 65, no. 4, Apr. 1960, pp. 1139-1150.

10-14. Garriott, Owen K.: The Determination of Ionospheric Electron Content and Distribution From Satellite Observations, Part 2, Results of the Analysis. J. Geophys. Res., vol. 65, no. 4, Apr. 1960, pp. 1151-1157.

10-15. De Mendoza, F.: Ionospheric Studies With the Differential Doppler Technique. Radio Astronomical and Satellite Studies of the Atmosphere, J. Aarons, ed., American Elsevier (Amsterdam), 1963, pp. 289-312.

10-16. Misyura, V. A.; Solodovnikov, G. K.; and Migunov, V. M.: Gradients of the Integral Electron Content in the Ionosphere. Geomagn. & Aeron., vol. 4, 1964, pp. 872-874. (Primary source—Geomagn. i Aeronomiya, vol. 4, 1964, pp. 1124-1126.)

10-17. Tyagi, T. R.: Determination of Total Electron Content From Differential Doppler Records. J. Atmos. Terrestrial Phys., vol. 36, July 1974, pp. 1157-1164.

10-18. Grossi, Mario D.; and Gay, Ray H.: Doppler Measurements of the Ionosphere on the Occasion of the Apollo-Soyuz Test Project. Part 1: Computer Simulation of Ionospheric-Induced Doppler Shifts. Special Rep. No. 366, Smithsonian Astrophysical Observatory (Cambridge, Mass.), July 10, 1975.

10-19. Gay, Ray H.; and Grossi, Mario D.: Doppler Measurements of the Ionosphere on the Occasion of the Apollo-Soyuz Test Project. Part II: Inversion of Differential and Rotating Doppler Shifts. Special Rep. No. 367, Smithsonian Astrophysical Observatory (Cambridge, Mass.), July 11, 1975.

10-20. King-Hele, Desmond: Theory of Satellite Orbits in an Atmosphere. Butterworths (London), 1964.

10-21. Gaposchkin, E. M., ed.: 1973 Smithsonian Standard Earth (III). Special Rep. No. 353, Smithsonian Astrophysical Observatory (Cambridge, Mass.), Nov. 28, 1973.

10-22. The American Ephemeris and Nautical Almanac for the Year 1975. U.S. Government Printing Office, 1973.

10-23. Grossi, M. D.: Spacecraft-to-Spacecraft Ionospheric Measurements on Occasion of the Apollo-Soyuz Test Project. Proceedings of the Beacon Satellite Investigations of the Ionosphere Structure and ATS-6 Data, Acad. Sci. USSR (Moscow), vol. 1, 1975, pp. 84-91.

10-24. Gay, R. H.; and Grossi, M. D.: The Ionospheric Experiment of the Apollo-Soyuz Test Project. Paper presented at the American Geophysical Union Meeting (Madison, Wis.), Sept. 1975.

10-25. Al'pert, Ja. L.: On Ionospheric Investigations by Coherent Radiowaves Emitted From Artificial Earth Satellites. Space Sci. Rev., vol. 18, 1976, pp. 551-602.